

Capillary levelling of immiscible bilayer films

CAPILLARY LEVELLING OF IMMISCIBLE BILAYER FILMS

BY

CARMEN LEE, B.Sc.

A THESIS

SUBMITTED TO THE DEPARTMENT OF PHYSICS & ASTRONOMY

AND THE SCHOOL OF GRADUATE STUDIES

OF MCMASTER UNIVERSITY

IN PARTIAL FULFILMENT OF THE REQUIREMENTS

FOR THE DEGREE OF

MASTER OF SCIENCE

© Copyright by Carmen Lee, August 2018

All Rights Reserved

Master of Science (2018)
(Physics & Astronomy)

McMaster University
Hamilton, Ontario, Canada

TITLE: Capillary levelling of immiscible bilayer films

AUTHOR: Carmen Lee
B.Sc., (Physics & Atmospheric Science)
Dalhousie University, Halifax, Canada

SUPERVISOR: Dr. Kari Dalnoki-Veress

NUMBER OF PAGES: viii, 60

Abstract

This is a ‘sandwich thesis’ consisting of a publication that I contributed to during my M.Sc. work. The thesis begins with an introduction section in Chapter 1 that discusses the relevant physical concepts to the work performed in the publication. These topics include, polymers in section 1.1, fluid dynamics in section 1.2, and capillary effects in section 1.3. Chapter 2 contains an experimental technique section that maps out the experiments performed in the manuscript.

The manuscript, Chapter 3, details the capillary driven levelling of thin polymer step that is supported by an immiscible polymer film and the dissipation of the capillary energy of the system. We find that the dissipation mechanism depends strongly on the viscosity ratio between the top and the bottom films. We developed a model of the energy dissipation that agrees well with the experimental results.

Acknowledgements

It's said that a grad student's relationship with their supervisor is the key factor to their happiness in grad school. Luckily for me, this was never a concern. Kari, thanks for being such a supportive, encouraging, and knowledgeable supervisor. My words don't come close to capturing all that you've helped me, but hopefully with a Ph.D I figure it out (4 more years!!!). Thank you so much, Kari.

Thanks to the KDV family, you folks are an amazing crew to work with. You are always great to bounce ideas off of, to share a beer with, or to come up with some lab shenanigans. A pleasure to share a lab with you!

A huge thank you to my family and friends. Your continued support of me and my endeavours in and out of the lab keeps a girl sane. A particular shout out to my fellow grad students (Jocelyn, Emma, Gill, John L., Thanassis, Clementine, Sarah E...). I love you all. Thank you.

I give no thanks to the ultra-pure water machine. Please stop breaking.

Contents

Abstract	iii
Acknowledgements	iv
1 Introduction	1
1.1 Polymers	3
1.1.1 Viscoelasticity	6
1.1.2 Glass transition temperature	8
1.1.3 Polymers at interfaces	9
1.1.4 Polymer interface width	11
1.1.5 Polymer interfacial energy	13
1.2 Fluid dynamics	13
1.2.1 Thin Film Equations	15
1.2.2 Flow profiles in the boundary layer	18
1.3 Capillary-driven levelling	20
1.3.1 Surface tension and surface energy	20
1.3.2 Laplace Pressure	22
1.3.3 Capillary length	24

1.3.4	Capillary energy and viscous dissipation	25
1.3.5	Capillary levelling and boundary conditions	29
2	Experimental Details	31
2.1	Substrate preparation	31
2.2	Spin coating	32
2.3	Floating films	33
2.4	Annealing and washing films	34
2.5	Atomic force microscopy	35
2.6	Ellipsometry	37
3	Capillary Levelling of a Liquid Stepped Film Supported on an Im-	
	miscible Liquid Film	38
3.1	Paper summary	38

List of Figures

1.1	a) An example of the overall structure of one linear polymer chain of polystyrene. The size of the polymer molecule can range from mere nanometers up to hundreds of nanometers in dimension, depending on polymer length. b) A close up on a section of the polystyrene to show the random walk structure of the molecule. c) A further close-up shows styrene monomers that are covalently bonded together	4
1.2	A schematic of two fluids that have phase separated. The interface shows the interfacial width for two phase separated polymers.	12
1.3	Schematic of a thin liquid film with the geometric coordinates indicated and the surface tension, γ , and viscosity, η , as noted. The top profile is stepped similarly to the geometry of the experiments performed in this thesis.	18

1.4	a) Velocity profile of Poiseuille flow in a thin liquid film with a no-slip boundary condition at $z = 0$ and a no-stress boundary condition at $z = z$. b) Velocity profile of plug flow in a thin liquid film with no-stress boundary conditions at $z = 0, z$. c) Velocity profile of Couette flow in a thin liquid film with a no-slip boundary condition at $z = 0$, and a no-slip boundary condition between the film at $z = z$ and the top plate, but with the top plate moving at velocity, v	19
1.5	a) A body of liquid that has had the surface perturbed away from equilibrium. b) A thin fibre of liquid suspended between two flexible supports. The liquid will pull on the supports with a force proportional to the surface tension.	21
1.6	Schematic of a droplet of water suspended in air with radius R . An imagined increase in radius, dR is outlined by the dashed line.	23
1.7	Schematic of capillary levelling of a liquid surface to a minimal energy state.	26
2.1	A schematic of the as-prepared sample, where the three layers are indicated with the given material. $h_{\text{PMMA-u}}$ indicates the thickness of the upper portion of the step, $h_{\text{PMMA-l}}$ indicates the thickness of the lower portion of the step, and h_{PS} indicates the thickness of the underlying liquid film.	34
2.2	Components of the atomic force microscope	36
2.3	Schematic of a Lennard-Jones or 6-12 potential to model interatomic attractions and repulsions.	36

Chapter 1

Introduction

Fluids flow. From the rivulets running down a car window to the global ocean currents, water flows over many scales. Air flows around you as you walk through a room. Hydrogen and helium form convective flow cells in the bodies of stars. Fluid dynamics is the fundamental study of all these types of flow, and more.

As with most fields of physics, counterintuitive behaviour happens at interfaces: this is also true for fluid dynamics. For example, a fluid flowing in a chamber will experience a boundary condition effect along the sides of the chamber. Fluids are often treated as a continuum - meaning the fluid body is treated as a single, continuous body [1]. A continuous fluid requires that the velocity inside a fluid must be continuous. Therefore, near a boundary, the velocity of the fluid must match the velocity of the boundary, and this results in a ~ 100 nm thick boundary layer that forms at the interface. The behaviour in the boundary layer can exhibit different properties than the bulk flow; however, they are difficult to study due to their small size [2, 3]. In this thesis, we will probe the dynamics within the boundary layer using thin liquid films with thicknesses on the same scale as the boundary layer. Surprisingly, we find

that continuum fluid dynamics works perfectly even on these small length scales, and we employ it to explain the results obtained in this thesis.

Fundamentally, thin films are subjected to the same forces that any simple liquid is subjected to. These forces include surface tension effects, which causes liquid to assume a minimal surface area. Evidence of this is seen when water beads up on skin after going for a swim, when water striders stay on top of the water, and even when salad dressing separates after it has been shaken up. Most liquids that we encounter in everyday life are difficult to study in the thin film geometry because they flow quickly and are not stable as thin films. For this reason, we use thin films fabricated out of polymers [4].

Polymers are perhaps the most diverse material found in everyday life. From the plastic of your water bottle, to the coating on your phone screen, to the DNA in your body, these molecules pervade every aspect of our life [5]. Thin polymer films are an active area of study because they have several key roles in technological applications, such as coatings for microelectronics or as thin adhesive layers [6]. Thin films have a large surface area to volume ratio. Typically, most of the material that makes up an object is contained within the bulk, but for thin films, the majority of the object is now the surface of the film. Properties of surfaces can be different than those of the bulk, and a good understanding of surfaces is essential to developing these technologies [7, 8]. One other useful physical property of a polymer is the ability to transition from a solid to a liquid with increasing temperature. Moreover, thin polymer films lend themselves to study fundamental physics questions, like what happens in the boundary layer of a fluid [6, 7, 9–12].

While flow of thin liquid films has been highly studied, several fundamental questions on the effects of the boundary condition still remain [13]. This thesis investigates how a liquid boundary condition affects the viscous flow profile in a thin liquid film through the use of capillary levelling. In Chapter 1, polymer properties, viscous flow and capillarity are discussed as they relate to the presented work. Chapter 2 discusses the experimental details of the work presented in the proceeding chapters. Chapter 3 is a manuscript which has been prepared for publication and contains the major results of this thesis. It is preceded by an introduction to the manuscript and my specific contributions to the research. In this manuscript, we examine capillary levelling of a viscous liquid step that supported by a less viscous liquid substrate.

1.1 Polymers

Polymers are used in this thesis because of their easily tuned physical properties. Polymers are ubiquitous in everyday life, and can be found in plastics, rubbers, and even the cellulose that composes the paper this thesis is printed on. Furthermore, DNA, RNA, and proteins are polymers that give rise to life. Polymers are a broad range of materials, but at their essence, polymers are macromolecules made from repeating subunits that are covalently bonded together [14]. Figure 1.1c) shows an example the repeating molecules or monomers for a common polymer, polystyrene. The monomers of polystyrene are called styrene and the covalent bonds between them allow for rotation along the chain, which directly results in a highly flexible chain [15].

When a polymer is in a liquid state, the polymer will exhibit a random walk due to the flexibility of the bonds [14]. Figure 1.1b) shows the scale of the random walks. The repeating units can form many different architectures, including linear

chains, branched chains, or stars [15]. In this thesis, I use linear, synthetic polymers. Linear polymers are polymers with monomeric units that are bonded together into a long flexible chain, similar in structure to a spaghetti noodle. Figure 1.1a) shows an example of the overall linear structure of a molecule of polystyrene, a polymer used in this thesis.

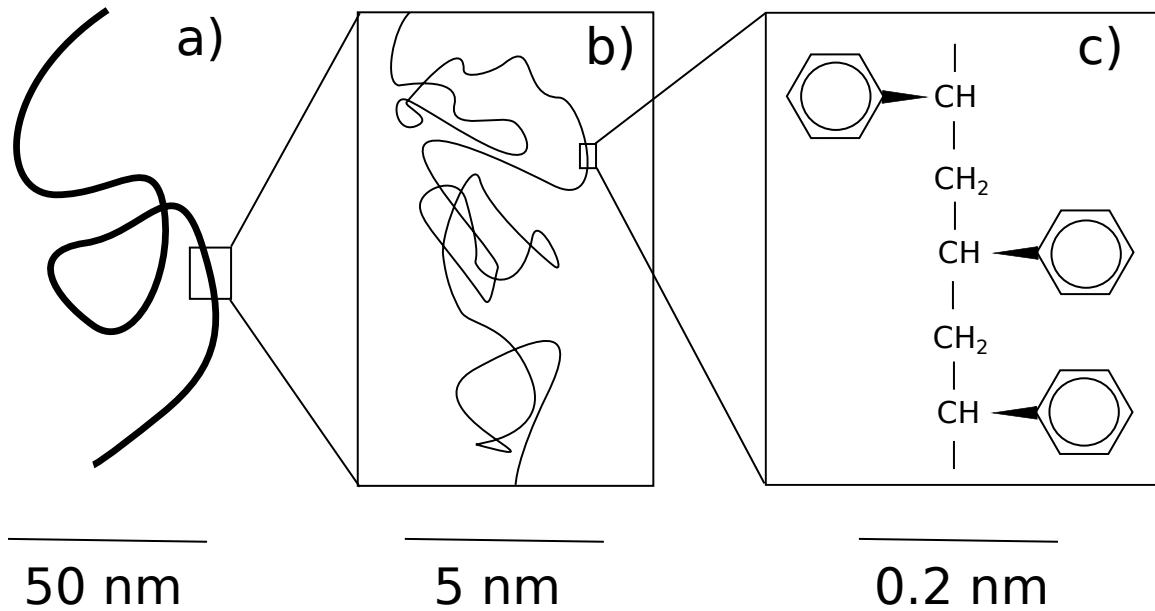


Figure 1.1: a) An example of the overall structure of one linear polymer chain of polystyrene. The size of the polymer molecule can range from mere nanometers up to hundreds of nanometers in dimension, depending on polymer length. b) A close up on a section of the polystyrene to show the random walk structure of the molecule. c) A further close-up shows styrene monomers that are covalently bonded together

The length of the polymer can be described by the total number of repeat units, denoted by N . Typical values of N can range from 10^3 - 10^6 . N , however, is a difficult value to measure directly. For a linear polymer, the length of the chain is proportional to the molecular mass of the polymer; the longer the molecule is, the more massive the molecule is. A way of measuring the length of polymers is to measure the molecular mass.

A typical ensemble of polymers will have chains with a variety of lengths. The variance in lengths is known as polydispersity. Due to the polydispersity of a sample of polymers, it is useful to measure the polymer ensemble as a whole by considering the average molecular weight of the ensemble. The number molecular weight, M_n , can be thought of as the first moment of the mass distribution [15]. The number molecular weight is defined as the total mass of the system divided by the number of molecules

$$M_n = \frac{\sum_i N_i M_i}{\sum_i N_i} = \sum_i n_i M_i, \quad (1.1)$$

where n_i is the number fraction of chains in the ensemble with molar mass, M_i . The weight average molecular weight, M_w , is the second moment of the mass distribution and it is defined in equation 1.2 [15]. The mass-weighted average is a different method of averaging and it will tend to put more emphasis on longer chains

$$M_w = \frac{\sum_i W_i M_i}{\sum_i W_i} = \sum_i w_i M_i, \quad (1.2)$$

where W_i is the weighting that is associated with the total mass for the i^{th} chain length. The weighting can be defined as $W_i = M_i N_i$. The weight average molecular weight can then be expressed in terms of the mass fraction, w_i . Although there are several ways of taking averages, the two defined above yield a useful quantity known as the polydispersity index (PI),

$$\text{PI} = \frac{M_w}{M_n} \geq 1. \quad (1.3)$$

The polydispersity index gives indication of the distribution of the sample of polymer. $PI = 1$ indicates that there is a perfectly monodisperse sample. For the work conducted in this thesis, all polymers had a $PI \leq 1.1$.

1.1.1 Viscoelasticity

At low temperatures, polymers form a glassy solid. In this state, the polymer chains do not possess enough kinetic energy to freely move past the confining molecules around them. The molecular movements are no larger than what is dictated by thermal noise. At high temperatures, these fluctuations become sufficiently large so the chains are free to escape the confining cage created by neighbouring polymers. At these temperatures, a polymer is free to move in response to an applied stress. If the stress occurs over a short time scale, the polymer will have an elastic response due to the polymer entanglement and the system acts as an entropic spring [15]. However, if the stress is applied over a long period of time, the chains have time to slip past each other, exhibiting viscous flow. In the work reported in this thesis, we work on the time scale where only viscous behaviour is exhibited, and the system can be treated as a simple viscous fluid.

The viscosity of a polymer melt is highly dependent on temperature [16]. Conceptually, one can imagine that as the temperature increases, the kinetic energy of the polymer molecules increases, giving them more energy to move and flow. When an external stress is applied to the polymer, the polymer will respond more quickly, and thus is less viscous. Likewise, lowering the temperature will cause the chains to respond more slowly, increasing the viscosity.

Conveniently, it has been observed that the flow behaviour of a polymer at a lower

temperature has the behaviour as the same polymer at a higher temperature; it just proceeds more slowly [15]. This relationship is known as time-temperature superposition. Time-temperature superposition is the general relationship between time and temperature for the viscoelastic properties of a polymer melt. For example, a polymer will flow the same amount at a certain temperature for a certain amount of time as it will for less time when it is at a higher temperature. Thus, the flow of a system can be probed over several orders of time scales by simply changing the temperature and then shifting the viscosity-time behaviour appropriately [16]. Viscoelastic behaviour can be rescaled by a simple shift along the time axis of viscosity-time plot at different temperatures. This shift is denoted by $a_T(T)$ [17]

$$a_T(T) = \frac{\eta(T)}{\eta(T_o)} = \frac{\tau(T)}{\tau(T_o)}. \quad (1.4)$$

This equation states that the viscosity, η , at a temperature, T , is equivalent to the viscosity at a reference temperature, T_o , with an addition of a shift. This shift is also valid for the characteristic time scale, τ , of the system. A variant on time-temperature superposition is the Vogel-Fulcher Law. The Vogel-Fulcher Law is an empirical law that describes the exponential relationship between viscosity and temperature for any viscoelastic material

$$\eta(T) = \eta_o \exp\left(\frac{T_A}{T - T_v}\right), \quad (1.5)$$

where T_A is an activation temperature (corresponding to an activation energy to induce motion), η_o is a reference viscosity and T_v is known as the Vogel temperature, which represents a shift in temperature. The three values are material dependent and

found empirically.

The Williams-Landel-Ferry equation (WLF) is an equivalent formulation to the Vogel-Fulcher Law. The WLF equation compares the known viscosity of a polymer at a reference temperature to an unknown viscosity at a different temperature. The WLF equation uses one single reference temperature, T_o

$$\frac{\eta(T)}{\eta(T_o)} = 10^{-C_1(T-T_o)/(C_2+T-T_o)}. \quad (1.6)$$

Although this relationship is true for many amorphous polymers and glass forming materials, it becomes particularly useful for polymers as C_1 and C_2 become almost universal when the reference temperature is the temperature when the polymer transitions from a solid to a liquid. The specifics of this temperature will be discussed in section 1.1.2.

1.1.2 Glass transition temperature

Many polymers are glassy solid materials at room temperature, but transition to the liquid melt state when heated. The temperature that the transition occurs at is the glass transition temperature. Unlike liquid water to ice, where the transition occurs at one distinct temperature (this type of transition is known as a first order phase transition), there is not a distinct glass transition temperature [18]. The glass transition temperature is often defined with respect to the viscosity of the polymer melt. As the temperature of the polymer is lowered, approaching the glass transition temperature, the viscosity increases to the point where relaxation is no longer possible on the experimental time scale. However, because experiment times vary, there is no clear definition where the cut-off should occur, as what can appear solid in one

experiment may still exhibit flow in a longer experiment.

The transition can be seen by examining the Vogel-Fulcher law, where there is a singularity in the viscosity when $T = T_v$ [17]. At this point, the viscosity is infinite and any feasible measurement of flow is beyond the experimental scale. As the system is cooled, the polymer becomes more and more sluggish until the glass transition temperature is reached and the system is frozen. This means that the polymer is solid. The two polymers used in this research, polystyrene and poly methyl(methacrylate), have glass transition temperatures of 100 °C and 105 °C, respectively [19].

1.1.3 Polymers at interfaces

When two liquids are mixed together, they will either form a homogeneous solution or they will separate into two different phases. An everyday example of phase separation is the way oil and water separate, barring any active mixing. The reason that liquids phase separate into two different regimes is due to entropic and enthalpic contributions to the free energy of the mixture. It is a competition between the entropic cost, S , of molecules organizing at the interface, and the energetic cost, U , from interactions between different molecules. The free energy of a liquid interface made of point-like molecules, F , can be described as [15]:

$$F = U - TS = \underbrace{\chi\phi_A\phi_B}_{\text{interaction energy}} + \underbrace{kT(\phi_A \ln \phi_A + \phi_B \ln \phi_B)}_{\text{entropy of mixing}}, \quad (1.7)$$

where χ is the interaction cost between molecule A and molecule B. ϕ_A and ϕ_B are the volume fraction of molecule A and B, respectively, for a system at temperature, T , and k represents the Boltzmann constant. If the interaction energy is above a

critical value, the free energy is minimized by creating A rich and B rich domains. If the interaction energy is below the critical value, entropy dominates and the fluids are homogenous.

Equation 1.7 must be altered slightly for a polymer, as it only accounts for a molecule that can be approximated as a spherical particle. For a solution of polymers, any given site will still be occupied by either an A or B particle, and this depends on only the volume fraction of the two species. However, the interaction energy is dependent on polymer length, N . A longer polymer will have more sites to have interactions with different molecules. As a result, the interaction energy should scale with N . The free energy for a polymer molecule in a solution containing two species is [15]

$$\frac{F_{\text{mol}}^{\text{poly}}}{kT} = \phi_A \ln \phi_A + \phi_B \ln \phi_B + N \chi \phi_A \phi_B. \quad (1.8)$$

It is more usual to consider the free energy of a single monomer unit, instead of a single polymer molecule. In this case, the free energy is split among the monomer units:

$$\frac{F_{\text{site}}^{\text{poly}}}{kT} = \frac{\phi_A \ln \phi_A}{N} + \frac{\phi_B \ln \phi_B}{N} + \chi \phi_A \phi_B. \quad (1.9)$$

The above expression is known as the Flory-Huggins equation, where the interaction energy now accounts for the length of the polymer chain. The critical interaction cost, χ_c , which determines whether or not the mixture will phase separate, is $2/N$. For most polymers, N is very large and the critical cost is very small. As a result, long polymers rarely form a two-phase mixture as the entropic cost is too high. Shorter

polymers that do phase separate have phases that are essentially pure, but also have an interface between that is not atomically smooth. Figure 1.2 shows a diagram of a polymer-polymer interface. Polystyrene and poly methyl(methacrylate) are the two types of polymers used in this thesis, which have a large enough interaction cost that they are immiscible.

1.1.4 Polymer interface width

A simple argument can be made to describe the penetration depth of one polymer phase into the other [15]. Polymer are long, flexible chains in a configuration that can be thought of as a random walk. If the polymers in a melt were forced to have an atomically sharp interface with another polymer melt, there would be a significant and specific rearrangement of the chains at the interface. The rearrangement would come at a large entropic cost. Therefore, there is an intermediate mixing zone at the interface. We presume that the interface is instead composed of interlocking loops, as depicted in Figure 1.2. The width of the interface, w , depends on the length of the loop, which scales as a random walk with the number of monomers in the loop. [15]

$$w \propto a\sqrt{N_{\text{loop}}}, \quad (1.10)$$

where N_{loop} is the number of monomers in the loop, and a is the length of the monomer unit. The interface energy is now on the order of the interaction energy of the loop

$$U_{\text{int}} \sim \chi N_{\text{loop}} kT. \quad (1.11)$$

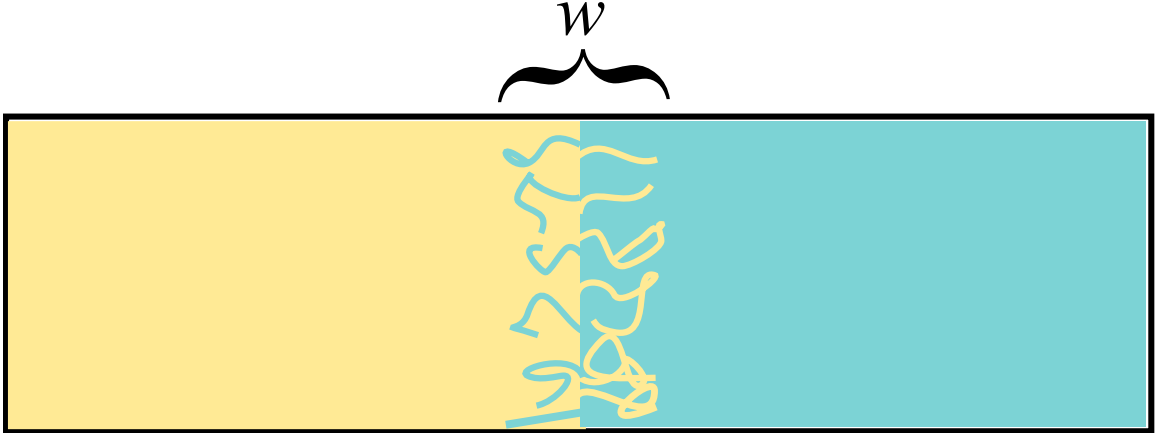


Figure 1.2: A schematic of two fluids that have phase separated. The interface shows the interfacial width for two phase separated polymers.

In equilibrium, the interface energy is approximately equal to the thermal energy or the interface itself would not be favourable or stable. As a result, equation 1.11 simplifies when considering the interfacial energy for one polymer excursion into the other phase

$$1 \sim \chi N_{\text{loop}}. \quad (1.12)$$

This expression can be combined with equation 1.10 to give an estimate of the width of the polymer-polymer interface in terms of the interaction cost and the monomer length

$$w \propto \frac{a}{\sqrt{\chi}}. \quad (1.13)$$

For most polymers, this is typically between 1-3 nm. This simple calculation predicts the overall behaviour of the interface width of two homopolymers to good approximation. This is further confirmed through more rigorous measurements from other

sources [20, 21]

1.1.5 Polymer interfacial energy

The interfacial energy of a phase separated polymer melt can be estimated by counting the number of unfavourable interactions in a unit area. Consider an area at a polymer-polymer interface, the loop of intertwining polymer will have length w , and width a . Each unique interaction between different polymer species will cost χkT per interaction, of which there are N_{loop} . Therefore, the interfacial energy, γ , can be calculated as the energy per area

$$\gamma = \frac{N_{\text{loop}}\chi kT}{wa}. \quad (1.14)$$

Using the derived values for w and N_{loop} from the previous section, the interfacial energy can be written in terms of measurable values

$$\gamma = \frac{kT}{a^2} \sqrt{\chi}, \quad (1.15)$$

showing that the interfacial energy of a polymer-polymer interface scales with the square root of the interaction cost.

1.2 Fluid dynamics

Fluid dynamics is a field of science which describes fluid flow over several orders of magnitude. There are different regimes where different governing equations are valid. The flow of an incompressible, viscous fluid, may generally be described by the Navier-Stokes equations [1]:

$$\nabla \cdot \mathbf{u} = 0. \quad (1.16)$$

$$\frac{\partial \mathbf{u}}{\partial t} + (\mathbf{u} \cdot \nabla) \mathbf{u} = -\frac{1}{\rho} \nabla p + \nu \nabla^2 \mathbf{u} + g, \quad (1.17)$$

where \mathbf{u} is the velocity vector, ρ is the density of the fluid, p is the pressure applied to the fluid parcel, ν is the kinematic viscosity of the fluid, and g is a body force acting on the fluid. Equation 1.16 states that the divergence of a volume of fluid with velocity, \mathbf{u} , must be equal to zero, where bolded symbols indicate vector quantities. For any incompressible fluid, the number of fluid particles that enter a defined volume, an equal number must exit.

The second part of the Navier-Stokes equations, equation 1.17, refers to the contributing factors to the flow of the fluid. The origin of the left side of equation 1.17 comes from conservation of momentum of the fluid parcel as it moves [22]. The term on the left-hand side of the equation, $\frac{\partial \mathbf{u}}{\partial t}$ is the acceleration term of the fluid parcel. It accounts for the simple linear acceleration that the fluid parcel has in the direction of motion. The next term, $(\mathbf{u} \cdot \nabla) \mathbf{u}$, is the inertia term [22]. The inertia term can be rewritten in the form of the two directional components, $(\mathbf{u} \cdot \nabla) \mathbf{u} = (\nabla \times \mathbf{u}) \times \mathbf{u} + \nabla(\frac{1}{2} \mathbf{u}^2)$. The resistance to rotational motion is represented by the first term, and the resistance to linear motion by the fluid is represented by the second term [1].

The right-hand side of equation 1.17 contains the driving forces that cause liquid motion. The first term, $-\frac{1}{\rho} \nabla p$ is the effect of pressure, p , acting perpendicular to the direction of fluid flow [22]. The second term accounts for the viscosity of the fluid, $\nu \nabla^2 \mathbf{u}$. A liquid with kinematic viscosity, ν , will exert shear and normal stresses from moving particles of a viscous liquid past each other. The final term of the equation,

g , is the inclusion of any external body forces that may act on the fluid. The Navier-Stokes equations capture the responses and driving terms of fluid flow. Although the Navier-Stokes equations are seemingly docile in this form, each vector quantity is three dimensional, meaning that equations expand into four coupled partial differential equations [1]. Exact, analytic solutions to these equations are currently only possible under simplified conditions. The next section considers one example of simplification, which will be used throughout this work.

1.2.1 Thin Film Equations

For many cases, the Navier-Stokes equations may be simplified based on the geometry of the system. To determine if the flow will be turbulent or laminar, one can consider the Reynolds number, Re , [1]

$$Re = \frac{UL}{\nu}. \quad (1.18)$$

Where U is the typical flow speed of a viscous fluid, L is the typical length scale and ν is the kinetic viscosity. The Reynolds number is the ratio between the inertia term and the viscous term of the Navier-Stokes equation,

$$\frac{\text{inertia term}}{\text{viscous term}} = \frac{(\mathbf{u} \cdot \nabla)\mathbf{u}}{\nu \nabla^2 \mathbf{u}} \sim Re. \quad (1.19)$$

A high Reynolds number, $Re \gg 1$, indicates a fluid with a small viscosity component relative to the inertial component. In this regime, the flow often becomes turbulent when it is subject to small perturbations. Fluids with low Reynolds numbers, $Re \ll 1$, will tend to non-turbulent flow as the viscous term dominates the inertial term. In the thin film equation, the fluid is assumed to have a low Reynolds

number so that the inertia terms of the Navier Stokes equation can be neglected in favour of the viscous terms. Furthermore, a thin film is expected to have much higher flow in the plane of the film than in the out of plane direction. This geometric condition gives rise to the lubrication approximation, where flow is assumed to be parallel to the plane of the thin film and non-linear terms of the flow may be neglected.

Thin liquid films with low Reynolds numbers are used in this thesis. Thin liquid films are geometries that are significantly thinner in one direction than the other two. Several simplifications of the Navier-Stokes equations are made by considering the geometric constraints. Furthermore, we assume that there are no external body forces acting on the film, as gravity effects are negligible - to be discussed later in this thesis. The liquid in the films is highly viscous and the inertia term may be neglected; therefore, the Navier-Stokes equations reduce to [1]:

$$-\nabla p + \eta \nabla^2 \mathbf{u} = 0, \quad (1.20)$$

$$\nabla \cdot \mathbf{u} = 0, \quad (1.21)$$

where η is the viscosity of the fluid and is related to the kinematic viscosity as $\eta = \nu\rho$. Further simplification of the Navier Stokes equations are performed when considering the geometry of the sample. Expanding the previous equations for Cartesian coordinates

$$\frac{\partial p}{\partial x} = \eta \left[\frac{\partial^2 u}{\partial x^2} + \frac{\partial^2 u}{\partial y^2} + \frac{\partial^2 u}{\partial z^2} \right], \quad (1.22)$$

$$\frac{\partial p}{\partial y} = \eta \left[\frac{\partial^2 v}{\partial x^2} + \frac{\partial^2 v}{\partial y^2} + \frac{\partial^2 v}{\partial z^2} \right], \quad (1.23)$$

$$\frac{\partial p}{\partial z} = \eta \left[\frac{\partial^2 w}{\partial x^2} + \frac{\partial^2 w}{\partial y^2} + \frac{\partial^2 w}{\partial z^2} \right], \quad (1.24)$$

$$0 = \frac{\partial u}{\partial x} + \frac{\partial v}{\partial y} + \frac{\partial w}{\partial z}, \quad (1.25)$$

where $\mathbf{u} = (u, v, w)$ and u, v, w are velocities in the x -, y -, and z -directions respectively. For a thin film, it can be assumed that $w \sim 0$ in comparison to u , as there is very little material in the z -direction available to flow. The lubrication approximation directly stems from the large difference in the x - and z -components of the velocity. We can also assume that the pressure in the z -direction stays constant in the thin layer of fluid, and therefore $\partial p / \partial z = 0$.

Here we consider the geometry relevant to the work performed in this thesis: a step of liquid. For a step of liquid, as shown in Figure 1.3, the symmetry of the step plays an important role. Symmetry dictates that there will be no driving pressure along the step (y -coordinate), and therefore $v = 0$. This means that u is the only component of the velocity with significant flow.

Since the velocity along the step is zero, the incompressibility condition, equation 1.25 reduces to:

$$\frac{\partial u}{\partial x} + \frac{\partial w}{\partial z} = 0. \quad (1.26)$$

Note that the $\partial w / \partial z$ term is not neglected here, as both the w and z term are considered small, but dividing one by the other results in a potentially relevant number.

Equation 1.22 is the only relevant term from the continuity equations. It too can be further reduced, as the step of liquid is symmetric, and there should be no change in the flow velocity with change in the y -direction. Therefore, the flow along the step

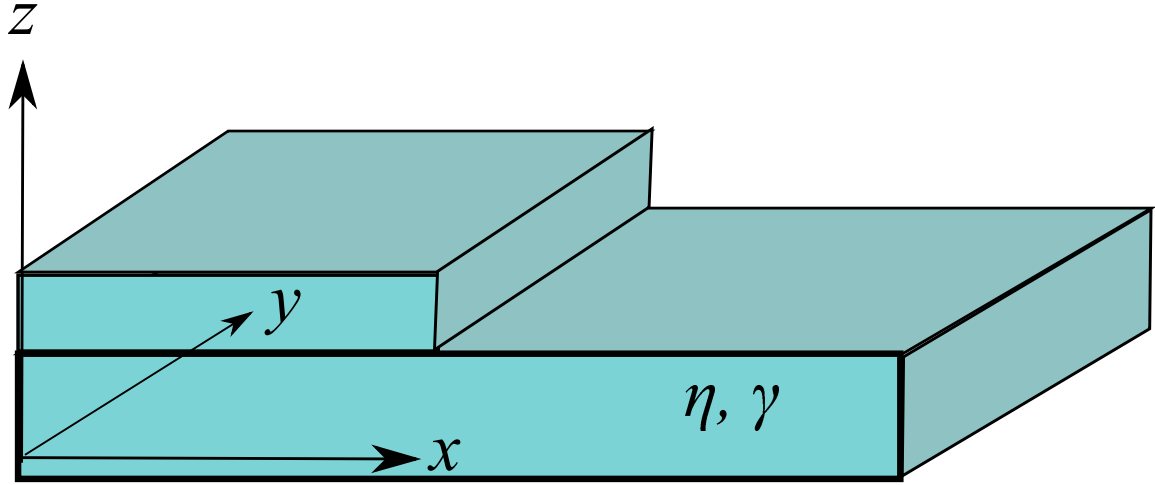


Figure 1.3: Schematic of a thin liquid film with the geometric coordinates indicated and the surface tension, γ , and viscosity, η , as noted. The top profile is stepped similarly to the geometry of the experiments performed in this thesis.

becomes [23]:

$$\eta \left(\frac{\partial^2 u}{\partial x^2} + \frac{\partial^2 u}{\partial z^2} \right) = \frac{\partial p}{\partial x}. \quad (1.27)$$

Equations 1.26 and 1.27 and the appropriate boundary conditions can be solved to describe flow in thin, viscous films [23].

1.2.2 Flow profiles in the boundary layer

To develop a full understanding of the type of flow that occurs in a thin film, we must understand the boundary conditions that are present. The boundary layer of a viscous liquid is usually ~ 100 nm. For thin films, the boundary layer takes up the entirety of the film. This is in contrast to bulk flow, where the boundary layer is a small but important portion of the flow.

In this thesis, we consider three types of flow that arise from different boundary conditions. A schematic example of each of these three flow profiles are shown in

Figure 1.4. Fig. 1.4a) is where there is a no stress interface at the fluid-air interface, and a no-slip condition at the fluid-solid interface. This results in Poiseuille flow. Poiseuille flow follows a parabolic increase in velocity starting with a zero velocity at the bottom, no-slip interface and with a smooth change to the maximum velocity at the top, no-stress interface. All flow is parallel to the substrate surface. Fig. 1.4b) is where there are two no-stress interfaces on either side of the fluid. This boundary layer flow is known as plug flow, where there is the same velocity along the thickness of the fluid. This is the same type of flow that occurs during the drainage of soap films and bubbles [24, 25]. Finally, Couette flow is depicted in Fig. 1.4c). This is where the top no-slip boundary moves relative to the bottom no-slip boundary. The velocity increases linearly from the bottom boundary to the top, in order to match the velocity of the top boundary.

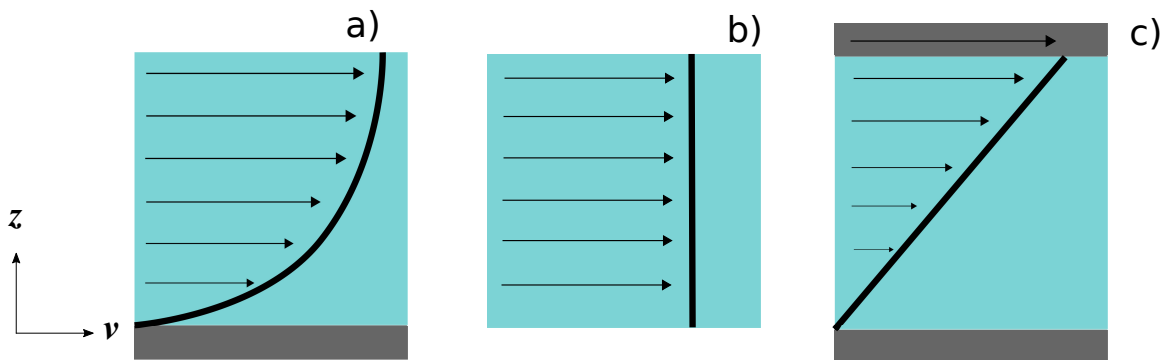


Figure 1.4: a) Velocity profile of Poiseuille flow in a thin liquid film with a no-slip boundary condition at $z = 0$ and a no-stress boundary condition at $z = z$. b) Velocity profile of plug flow in a thin liquid film with no-stress boundary conditions at $z = 0, z$. c) Velocity profile of Couette flow in a thin liquid film with a no-slip boundary condition at $z = 0$, and a no-slip boundary condition between the film at $z = z$ and the top plate, but with the top plate moving at velocity, v .

1.3 Capillary-driven levelling

When a liquid surface is perturbed from the equilibrium geometry, generally two forces will drive it back to equilibrium. Imagine it is early in the morning and the honey, which has been sitting overnight, is ready to be spread on some toast. As the honey is moved from the jar onto the toast, the surface of the honey in the jar is perturbed and it is no longer flat. Slowly the perturbation will flow in order to level the honey back to the equilibrium configuration. If the perturbation is large, there will be enough honey displaced out of equilibrium so the gravitational potential energy has been significantly changed. Gravity will work to establish equilibrium again. However, if the perturbation is small, the potential energy will not be significantly altered, but the surface energy has still changed. The honey will still level at this scale, but it is driven by surface tension. Levelling at this scale is known as capillary levelling [26]. We utilize capillary levelling in the work presented in this thesis.

There are three concepts that must be explained before capillary-driven levelling can be understood. Two are physical properties of the liquid, the surface tension and the capillary length. The third depends on the geometry of the liquid surface: the Laplace pressure.

1.3.1 Surface tension and surface energy

A liquid in equilibrium will have a minimal surface area. A soap bubble, for example, will form a perfect sphere. Water in a fish bowl will have a smooth, unwrinkled surface, provided the fish is not swimming too quickly. Any liquid in equilibrium will minimize the surface area by creating a ‘taut’ surface as though there were an overall tension applied to it. A perturbed liquid surface will be driven back to equilibrium

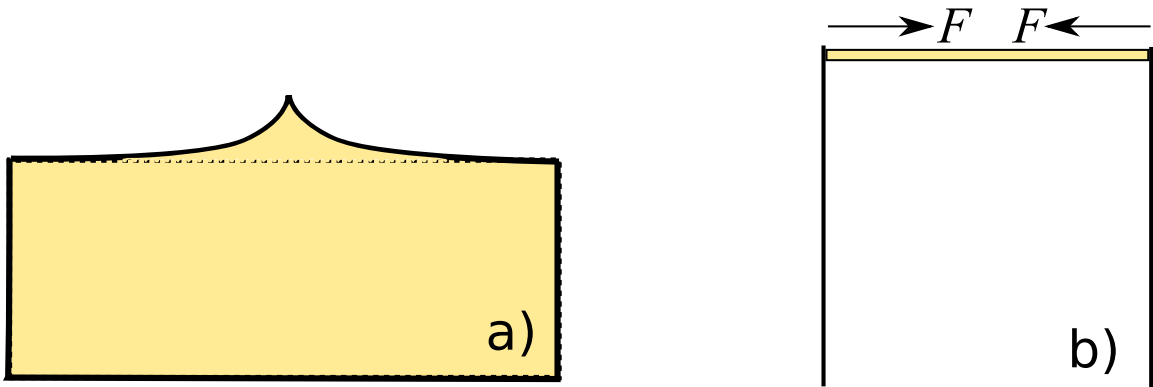


Figure 1.5: a) A body of liquid that has had the surface perturbed away from equilibrium. b) A thin fibre of liquid suspended between two flexible supports. The liquid will pull on the supports with a force proportional to the surface tension.

in a similar way to an elastic surface under tension. It is fairly easy to surmise why the system will be driven to the minimal surface area. Molecules in a homogenous liquid have the most favourable energetic interactions when they associate with the same type of molecules. This is why a liquid is cohesive instead of repulsive. If a molecule were to be brought to an interface with another liquid or gas, it loses half of the low energy, cohesive interactions, and more energetically costly interactions are formed with the other medium. In order to decrease the amount of unfavourable interactions, the liquid will change shape to minimize the surface area. The energy cost associated with the unfavourable interactions contributes to the surface energy.

Surface tension is similar to the surface energy of a liquid. Molecules at the surface have intermolecular forces that are associated with a difference in the number of cohesive bonds with other molecules. Surface tension may be reported as an energy per unit area or as a force per unit length. From a mechanical point of view, one can consider surface tension, γ , as the amount of work, W , that is required to distort a surface by a unit area, A , $\gamma = \partial W/dA$ [27]. For example, if a surface is distorted,

as shown in Figure 1.5 a), work is done on the liquid in order to add enough energy to the system to create more liquid-air interface. For the materials used in this thesis, the surface and interfacial tensions are $\gamma_{PS-air} = 31.34$ dyn/cm, $\gamma_{PMMA-air} = 31.22$ dyn/cm, and $\gamma_{PS-PMMA} = 1.65$ dyn/cm [28]. Another way of considering surface tension is to have a one-dimensional liquid, a fibre of liquid, that is suspended between two flexible supports as shown in Figure 1.5b). The liquid fibre will contract to minimize the surface area and in doing so, will pull the two supports together. This applies a force to the supports as a function of the distance pulled, $F = 2\gamma l$.

1.3.2 Laplace Pressure

A consequence of surface tension is that a volume of liquid will be driven to form a droplet to have the minimal surface area. In doing so, an outward facing pressure is created within the droplet. The pressure difference between the droplet and the medium is known as the Laplace pressure [24]. The Laplace pressure in the droplet arises due to the surface tension of the liquid and the curvature of the interface. To prove this claim, consider a spherical drop of water with radius, R , that is in the air. A schematic is shown in Figure 1.6. In order to change the interface by the amount dR , work must be done on the droplet to create more interface. The existing pressures and the capillary force will resist the change, as a result a simple mechanical work argument can be made

$$\partial W = -p_w dV_w - p_a dV_a + \gamma_{wa} dA. \quad (1.28)$$

The total work on the system depends on the pressure-volume work, $-pdV$, where the pressure, p , for the water (denoted with subscript w) and air (denoted with subscript

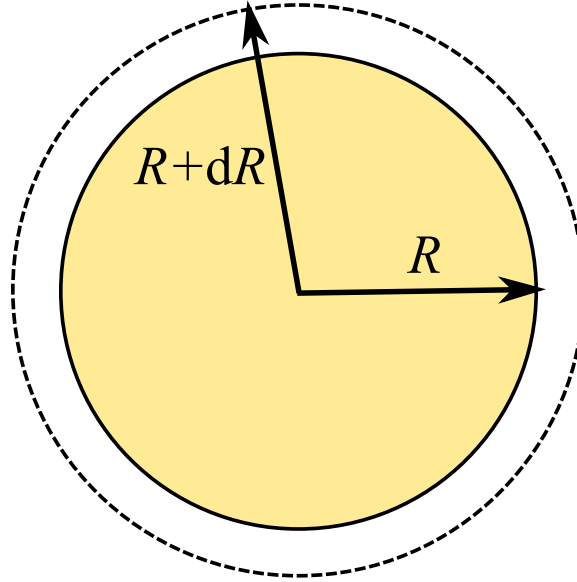


Figure 1.6: Schematic of a droplet of water suspended in air with radius R . An imagined increase in radius, dR is outlined by the dashed line.

a), and the volumetric change, dV . Additional work is associated with the surface tension, $\gamma_{wa}dA$. The volume change for the droplet can be related to the change in radius, $dV_w = 4\pi R^2dR = -dV_a$, as can the change in surface area, $dA = 8\pi R dR$. For the system to be in mechanical equilibrium, there is no change in work resulting in

$$\Delta p = p_w - p_a = \frac{2\gamma_{wa}}{R}. \quad (1.29)$$

This means that the Laplace pressure of a droplet with a small radius of curvature will be larger than a droplet with a larger radius of curvature [24].

This exercise was done for a perfect sphere; however, it can be generalized to any curved surface. The local curvature, C , is dependent on the two radii of curvature, R and R' , in orthogonal directions to the surface, $C = 1/R + 1/R'$. The Laplace pressure for any point on a curved surface is

$$\Delta p = \gamma C. \quad (1.30)$$

The local Laplace pressure can be fully predicted by both the surface tension and the curvature of the interface. Laplace pressure gradients on the same surface (areas of high and low curvature) will induce flow in order to relieve the pressure differences.

1.3.3 Capillary length

The capillary length, κ^{-1} , of a fluid interface indicates the typical length-scale for a system where both gravitational and surface tension effects are comparable in magnitude. A very good visual example of the capillary length is the meniscus that is present around a water glass. Capillary forces pull the surface of the water up around the edge of the glass, but after a certain length, gravity takes over to push the water to a flat surface. The distance between the edge of the glass and where the meniscus fades away is indicative of the capillary length. The gravitational effects are described by the hydrostatic pressure, which is the pressure associated with a parcel of liquid submerged at depth, κ^{-1} , in a liquid of density ρ , while in earth's gravity, g . The hydrostatic pressure is counteracted by the Laplace pressure due to the surface tension of the liquid. The Laplace pressure is estimated using equation 1.30, with the curvature being on the order of the capillary length. A simple calculation can be done when the two pressures are equal, [24]

$$\frac{\gamma}{\kappa^{-1}} = \rho g \kappa^{-1}. \quad (1.31)$$

A simple rearrangement yields an expression for the capillary length

$$\kappa^{-1} = \sqrt{\gamma/\rho g}. \quad (1.32)$$

For most liquids, the capillary length is on the order of millimeters, which sets the characteristic length scale of the system. Below this length, any perturbations or features will be subject to capillary forces. Above this length, gravity will act to level the surface. The length scale of the experiments performed in this thesis are well below the capillary length of both polymers and therefore gravitational effects can be neglected [29].

The driving force that acts on a liquid surface with perturbations below the capillary length stems from the surface tension. The levelling that occurs in this regime is known as capillary levelling and it is the method used to initiate flow in the experiments in Chapter 3.

1.3.4 Capillary energy and viscous dissipation

As discussed in the section 1.3.1, there is an energetic cost to creating a liquid interface. A liquid system has a minimal surface area, S_o , that has a minimal surface energy, E_o , associated with it. As a surface is perturbed away from the equilibrium configuration, there is additional energy known as the capillary energy. Figure 1.7 shows a surface with topographic roughness and surface area, S , and after some time the surface levels, reducing the surface area and thus, the capillary energy. The capillary energy is defined as the difference in surface energy from the current state to the minimal state

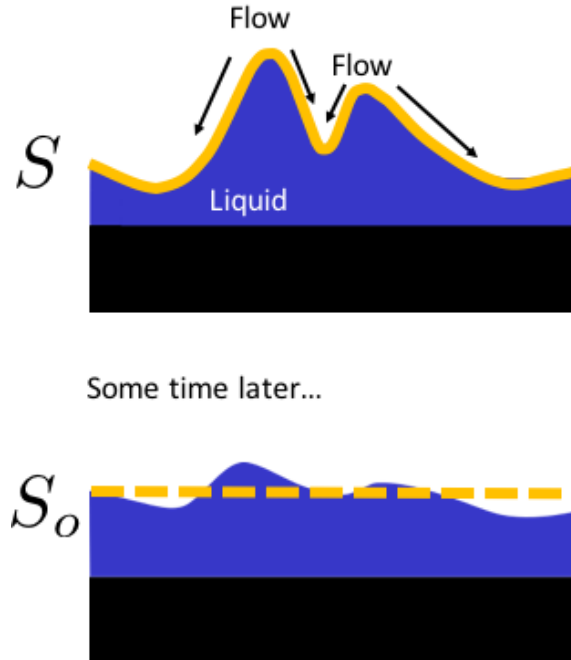


Figure 1.7: Schematic of capillary levelling of a liquid surface to a minimal energy state.

$$E_{\text{cap}} = E - E_o = \gamma(S - S_o), \quad (1.33)$$

where E and S are the energy and surface area of the perturbed fluid. A liquid system will transition from the high energy state to the low energy one. In order to do so, it dissipates the excess capillary energy to transfer the energy out of the system. In the case of thin liquid films, capillary energy is decreased through viscous dissipation.

Viscosity is the friction felt between molecules in a fluid as they move past one another. The higher the coefficient of friction between the molecules, the more viscous the fluid will be and the longer it will take to respond to an external stress. When a viscous fluid flows in response to a stress, the internal friction will work to dissipate some of the excess kinetic energy. In fluid dynamics, the boundary layer is where

viscous dissipation occurs because of gradients in flow velocity induce relative motion between the molecules. Consider a parcel of liquid that possesses kinetic energy, U , [1]

$$U = \frac{1}{2} \int_V \rho u_i^2 dV, \quad (1.34)$$

where u_i is the speed of each molecule of the liquid in a volume, V , and with density, ρ . By taking the derivative of the above equation with respect to time, the expression becomes

$$\frac{\partial U}{\partial t} = \int_V u_i \frac{Du_i}{Dt} \rho dV, \quad (1.35)$$

where Du_i/Dt indicates a 3-dimensional rate of change of the velocity of the fluid. Cauchy's equation of motion is $\rho Du_i/Dt = \partial T_{ij}/\partial x_j + \rho g_i$, where T is the stress tensor and the g is the body force [1]. Inserting Cauchy's equation of motion into equation 1.35 yields two separate integrals

$$\frac{\partial U}{\partial t} = \int_V \rho g_i u_i dV + \int_V u_i \frac{\partial T_{ij}}{\partial x_j} dV. \quad (1.36)$$

The second integral can be further broken down with integration by parts and the introduction of the stress tensor vector, $t_j = T_{ij} \cdot n_j$. This splits the change in kinetic energy into two volume integrals and one surface integral

$$\frac{\partial U}{\partial t} = \int_V \rho g_i u_i dV + \int_S u_i t_j dS - \int_V \frac{\partial u_i}{\partial x_j} T_{ij} dV. \quad (1.37)$$

The third term indicates a summation over the indices. For an incompressible Newtonian fluid the stress tensor is symmetric and therefore the summation over the stress

tensor can be split into two

$$T_{ij} \frac{\partial u_i}{\partial x_j} = \frac{1}{2} T_{ij} \left(\frac{\partial u_i}{\partial x_j} + \frac{\partial u_j}{\partial x_i} \right). \quad (1.38)$$

Furthermore, the stress tensor for a simple Newtonian fluid is a function of the shear rate, $T_{ij} = \eta \frac{\partial u_i}{\partial x_j}$, $i \neq j$. The indices only account for shear rate and do not include pressure applied normal to the direction of flow. If we substitute the shear rate into the right-hand side of equation 1.38 and invoke the incompressibility condition $0 = \partial u_i / \partial x_i + \partial u_j / \partial x_j + \partial u_k / \partial x_k$, it reduces to

$$T_{ij} \frac{\partial u_i}{\partial x_j} = \frac{1}{2} \eta \left(\frac{\partial u_i}{\partial x_j} + \frac{\partial u_j}{\partial x_i} \right)^2 = 2\eta e_{ij}^2, \quad (1.39)$$

where $e_{ij} = 1/2 \left(\frac{\partial u_i}{\partial x_j} + \frac{\partial u_j}{\partial x_i} \right)$ and is the strain rate tensor. This equation relates the stress tensor to the viscous dissipation of energy. One can see that it will only be zero if the fluid particle does not change shape, meaning that there is no shear being applied to the parcel. The final expression for the change in energy with time can be expressed as

$$\frac{dU}{dt} = \underbrace{\int_V \rho \vec{g} \cdot \vec{u} dV}_{\text{potential energy}} + \underbrace{\int_S \vec{u} \cdot \vec{t} dS}_{\text{surface stresses}} + \underbrace{2\eta e_{ij}^2}_{\text{viscous dissipation}}. \quad (1.40)$$

For a thin film, the potential energy and surface stress terms are negligible, leaving the viscous dissipation term. Based on the same arguments that were made in the thin film equation section, section 1.2.1, the rate of strain tensor is only significant

for e_{jk} , as this is the only direction with significant gradients in viscosity,

$$\frac{dU}{dt} = \int \eta (\partial_z v)^2. \quad (1.41)$$

The capillary energy of a step dissipates by converting the capillary energy to kinetic energy through flow, which then loses energy via viscous dissipation [30]

$$\frac{dE_{\text{cap}}}{dt} = \int \eta (\partial_z v)^2. \quad (1.42)$$

This equation can now be solved using Stokes and Laplace flow [23]. The full analysis of energy dissipation for the system studied in this thesis can be found in Appendix B of the paper that is in Chapter 3.

1.3.5 Capillary levelling and boundary conditions

The ultimate goal of the research performed in this thesis is to examine how a liquid-liquid boundary condition affects the flow profiles. In the current literature, there is discussion over the influence of the liquid-liquid boundary [11, 31–35]. We chose to use capillary levelling of a thin polymer step to probe the flow mechanism. Capillary levelling has been shown in previous works to indicate the type of flow by solving the thin film equation for the appropriate boundary conditions [36–38]. The models and experimental data both have self-similar profiles, where the levelling profiles may be rescaled with respect to time using an appropriate scaling term. With capillary levelling of a liquid on a solid substrate, the capillary energy scales as a power law with respect to time [39]. In this case, the power law is $t^{-1/4}$ [30, 40, 41]. The thin film equation solved for the appropriate boundary conditions results in a Poiseuille

flow profile. For capillary levelling of a free-standing liquid film, the energy scales with a different power law, $t^{-1/2}$ [36, 42]. The flow profile is plug flow as outlined in the fluid dynamics section (no stress boundary conditions at both interfaces). The boundary conditions strongly affect the viscous flow and therefore the resulting energy dissipation. In the following chapters of this thesis, we demonstrate capillary levelling of a viscous polymer step while it is being influenced by a liquid-liquid boundary condition. Furthermore, we track the energy dissipation in the polymer step and in the underlying liquid.

Chapter 2

Experimental Details

This chapter elaborates on the experimental details and procedures discussed in the manuscript in Chapter 3. The research performed in this thesis was done with the utmost emphasis on lab cleanliness and all sample preparation was performed in a laminar flow hood to reduce dust. The following sections are presented in the order required to carry out the experiment.

2.1 Substrate preparation

Two main substrate types are used in this experiment. The first is silicon with a 5 nm layer of native oxide on the surface. The wafer is gently laid face down onto a lens tissue, and a diamond scribe is used to score lines parallel to the crystal planes in a 1×1 cm grid. The scribed lines are placed over a thin metal rod and pressure is applied on either side to encourage the silicon to break along the lines. During cleaving, newly separated pieces of silicon are moved to clean areas of lens tissue to prevent silicon dust from contaminating the surfaces. The square substrates are

sprayed with compressed nitrogen to remove large pieces of silicon dust that may have come into contact with the clean surface.

The other substrate is mica. Mica is a crystal structure that forms sheet-like planes with perfect cleavage between the atomic planes. These planes allow the mica to be easily cleaved to create a atomically flat surfaces. For this research, 1×1 inch squares of mica were cleaved by wedging a scalpel blade between two planes at one of the corners of the square. The separated corner is simply pulled apart with tweezers resulting in two atomically smooth mica surfaces. The dual substrates are dusted with compressed nitrogen to remove any mica particles that may have come into contact with the surfaces.

2.2 Spin coating

Spin coating is a fast and reliable method to create thin uniform polymer films. The process begins by dissolving the polymer into a solvent. In this thesis, polystyrene (PS) and poly-methyl(methacrylate) (PMMA) were dissolved in toluene. The concentration of the solutions ranged from 1.5% to 5% by mass. The PMMA molecular weight, $M_w = 56$ kg/mol, was not varied during the experiment (Polymer Source, Inc., polydispersity index ≤ 1.08). The molecular weights of the PS were 53.3, 106, 183, and 758.9 kg/mol (Polymer Source, Inc. and Scientific Polymer Products, Inc., polydispersity index ≤ 1.06). Solution is deposited onto a substrate and the substrate is rotated at speeds ranging from 1000 - 5000 rpm. The rotation causes the liquid to spread to coat the substrate, with excess material rolling off of the substrate, until a thin layer has formed. The layer continues to thin due to evaporation of the solvent until the film vitrifies [43]. Films are spun onto either mica or silicon. To drive off

the trapped solvent and to relax the polymers in the films, samples are annealed on a heating stage (Linkam) at 150 °C, which is above the glass transition temperature (100 °C for PS and 105 °C for PMMA) for 10 minutes. Film thicknesses were confirmed with ellipsometry and atomic force microscopy, which are described in sections 2.5 and 2.6.

2.3 Floating films

For the geometry used in this thesis, a film of PS was layered under two films of PMMA, with the top film of PMMA been fractured to create the step. Figure 2.1 shows a schematic of the desired geometry, with the thicknesses of the three layers indicated as $h_{\text{PMMA-u}}$, $h_{\text{PMMA-l}}$, and h_{PS} to indicate the upper PMMA, lower PMMA and PS film thicknesses, respectively. This system requires multiple thin films to be layered on each other. To do this, we employ a technique that involves floating the films on a clean water bath. A water bath is prepared with ultra-pure water (18.6 M Ω cm).

A thin film that has been spin-coated onto a mica substrate can be removed from the substrate and ‘floated’ onto the surface of the water bath. This is done by scoring the film with a scalpel blade, roughly 1 mm from the edge, and carefully lowering the film and substrate into the water at a shallow angle. Mica is hydrophilic and as the film is submerged, water will move between the hydrophobic polymer and the mica. This will detach the polymer film and leave it floating on the surface of the water. The film is now free for another polymer film that is supported on a silicon substrate (the films adhere more strongly to silicon and will not float off as they do for mica) to carefully lift it up out of the water. The two can be annealed at 70 °C (below

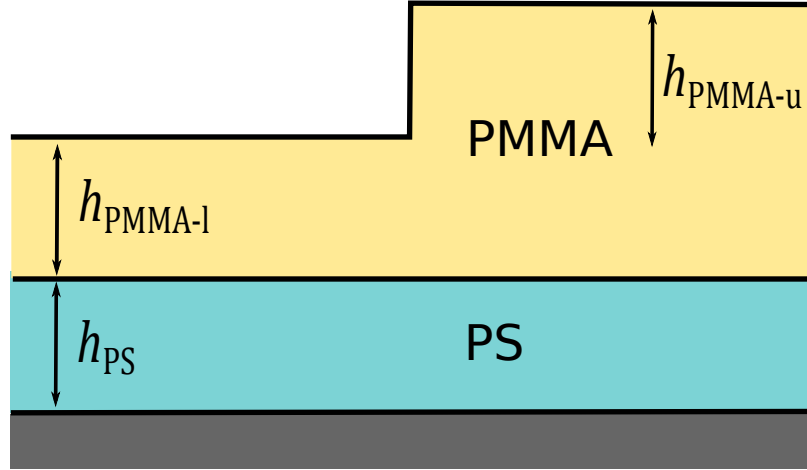


Figure 2.1: A schematic of the as-prepared sample, where the three layers are indicated with the given material. $h_{\text{PMMA-u}}$ indicates the thickness of the upper portion of the step, $h_{\text{PMMA-l}}$ indicates the thickness of the lower portion of the step, and h_{PS} indicates the thickness of the underlying liquid film.

the glass transition temperature of both polymers) to drive off excess water trapped between the two films.

The floating process can be repeated for a second film of polymer, but this time with the intention of creating a step-edge. If the polymer composing the film is sufficiently close to the entanglement molecular weight, the film will fracture cleanly into half when the film is agitated. The resulting halves can be lifted again out of the water to create a step with the lower film. The initial profile of the step was taken using atomic force microscopy (AFM).

2.4 Annealing and washing films

The samples were annealed well above the glass transition temperature, T_g , of both polymers. Above T_g , the layers flow as simple Newtonian fluids in response to the excess capillary energy stored by the step. In this thesis, the samples were annealed

on a heating stage (Linkam) at either 150, 165, or 180 °C. The samples were annealed for a period of time, and quenched back to room temperature so the polymers return to the solid-glassy state. AFM profiles were then taken to examine the topography of the PMMA and air interface. For some samples, the PMMA was washed off using a selective solvent ($\sim 66\%$ acetic acid and $\sim 33\%$ ultrapure water) by submerging it in the solvent and then rinsed with ultrapure water. The PS layer remained and AFM profiles were taken at the same location as before to examine how the two interfaces develop in tandem.

2.5 Atomic force microscopy

The atomic force microscope (AFM) is a powerful imaging tool that is used to examine topographical data on the nano- and microscale. Figure 2.2 shows a schematic of the components of the AFM. AFM works on the same principle as a record player, just on a much smaller scale. A finely pointed tip, with a tip's width as narrow as 10 nm, is supported by a flexible cantilever. A piezoelectric controller precisely positions the sample stage. A laser targets the back of the tip and is reflected back to a spatially resolved photodetector. As the tip is brought closer to the sample, it approaches a energy minima dictated by the Lennard-Jones potential. Figure 2.3 is a schematic of the potential, where there is a long range attractive van der Waals force (r^{-6}) and a short range repulsive force due to the Pauli exclusion principle (r^{-12}). In the most common form of AFM operation, the tip moves along the sample and it will remain the same distance away from the sample, regardless of topography, in order to stay at the energy minima. The tip accurately tracks the height of the sample as it is moved relative to the surface. When the tip is moved up and down, it causes the

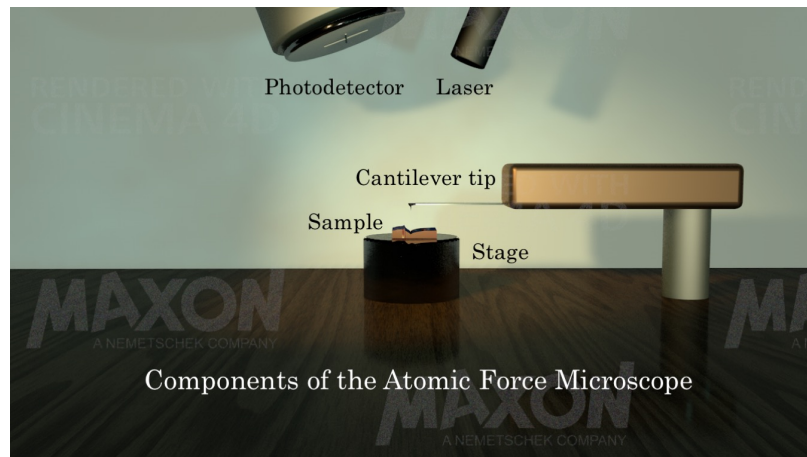


Figure 2.2: Components of the atomic force microscope

cantilever to bend and flex, which in turn causes the laser to reflect to a different location on the photodetector. The change in position on the photodetector provides the topological data along the sampled line. The AFM can raster back and forth to create a 3-dimensional map of the surface of the sample.

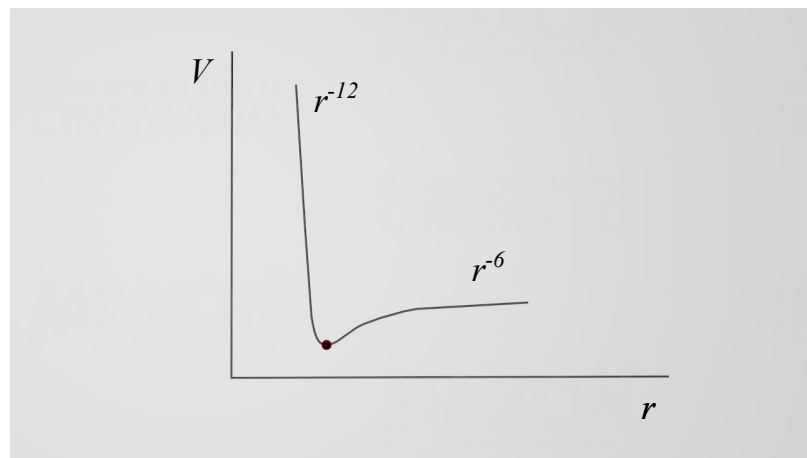


Figure 2.3: Schematic of a Lennard-Jones or 6-12 potential to model interatomic attractions and repulsions.

2.6 Ellipsometry

Ellipsometry is a non-invasive method of measuring the thickness of thin films. Ellipsometry, at its essence, is a technique that uses the in properties of light that is reflected off a thin film sample to determine the sample's thickness and refractive index. The ellipsometer used in this project (EP3, Accurion) employs a technique known as nulling ellipsometry. Specifically, a beam of elliptically polarized light with known polarization is incident on a thin film. Elliptically polarized light is where a linearly polarized beam of light is combined orthogonally with anywhere from $0^\circ < \theta$, 90° phase shift relative to one another. When the elliptical light is reflected off of the film, the p- and s- components (in plane and perpendicular to the plane of reflection) of the light are altered as it interacts with the film. For any thin film, a certain elliptical polarization will reflect as a linearly polarized light. An orthogonally oriented linear polarizer can completely extinguish the incident light. The ellipsometer changes the polarization of the incident light and the angle of the linear polarizer to find a minimum in light intensity. A model can be developed based on the polarization state of the incident and reflected light with fitting parameters to obtain the thickness and refractive index of the thin film.

Chapter 3

Capillary Levelling of a Liquid Stepped Film Supported on an Immiscible Liquid Film

3.1 Paper summary

In this chapter, I present a manuscript in preparation to be published in a peer reviewed journal. This paper addresses the effect of a liquid-liquid boundary condition on fluid flow in thin films. We prepare samples with a stepped polymer film layered on top of a thin film composed of a different polymer. We then follow the evolution of the top polymer-air interface and the bottom polymer-polymer interface as the samples are annealed above the glass transition temperature of both polymers. In this case, the top film was more viscous than the bottom film. From the profiles, we calculate the capillary energy, which is proportional to the area of the interface, of each interface and examine how they change with time. Furthermore, we varied

the viscosity ratio between the two films to study the different ways the energy is dissipated. We developed a viscous dissipation model to explain the decrease in capillary energy over time, and experimental results agree well with the model.

This project was motivated by previous work done on different stepped film geometries and the useful probe into boundary layer flow that they provide [37, 44, 45]. In collaboration with my supervisor, I designed and performed the experiment, as detailed in the manuscript. I also wrote the data analysis programs in Python. I performed preliminary development of the theoretical model. Vincent Bertin further refined and perfected the model and aided in some of the experiments. The manuscript was a collaboration between the authors. I prepared the experimental section and the figures, while V. Bertin wrote the theoretical section and appendices. We collaborated together on the remaining sections. As the work depends heavily on both the theoretical and experimental contributions, V. Bertin and I share ‘first authorship’ on this paper.

Capillary Levelling of a Liquid Stepped Film Supported on an Immiscible Liquid Film

Carmen Lee,^{1,*} Vincent Bertin,^{2,*} Thomas Salez,^{3,4} Elie Raphaël,² and Kari Dalnoki-Veress^{1,2,†}

¹*Department of Physics and Astronomy, McMaster University,
1280 Main Street West, Hamilton, Ontario, L8S 4M1, Canada*

²*Laboratoire de Physico-Chimie Théorique, UMR CNRS Gulliver 7083,
ESPCI Paris, PSL Research University, 10 rue Vauquelin, 75005 Paris, France*

³*Univ. Bordeaux, CNRS, LOMA, UMR 5798, F-33405 Talence, France*

⁴*Global Station for Soft Matter, Global Institution for Collaborative
Research and Education, Hokkaido University, Sapporo, Japan*

Flow in thin films is highly dependent on the boundary conditions. Here, we study the effect of a sharp liquid/liquid interface when flow is induced by capillary forces in a bilayer film. A stepped film is placed on another immiscible and less viscous film. The Laplace pressure gradient resulting from the curvature of the stepped film induces flow, and in doing so dissipates the capillary energy of the step. The effect of different viscosity ratios between the stepped film and the underlying film is investigated. A model is developed which describes the energy dissipation of viscous flow that occurs in each layer. The experimental and theoretical model are in good agreement. We find that the flow is initially dominated by plug flow in the top film before crossing over to Couette-like flow in the bottom film. The crossover time depends on the viscosity ratio between the two liquids.

I. INTRODUCTION

In the field of fluid dynamics, boundary condition effects are an active area of study. This is especially true in the context of thin liquid films, where the thickness of the film approaches the size of the boundary layer [1]. A question of particular interest is how boundary conditions affect the overall dynamics of a thin liquid film. Seminal work by de Gennes and Brochard-Wyart examined the interface between two polymer melts and predicted a discontinuity in the velocity across the interface. This is known as slip which can occur if the width of the interface is smaller than the entanglement length of both polymers [2–4]. Molecular dynamics simulations have confirmed the presence of slip at a sharp interface, as well as the resulting velocity profiles, and have been extended to simple immiscible liquids [5–7]. The effect of liquid/liquid boundary conditions is relevant for applications like the stability of thin polymer films for coatings [8], as well as in industrial processes like coextrusion of two liquids [9].

Capillary driven levelling occurs when there is excess interface which can be relaxed by smoothing any perturbations at the interface e.g. a thin film with some surface feature: a bump, a valley, etc. This levelling is a useful tool for studying fluid flow in nanometric thin films and is dependent on the boundary conditions and the material properties of the liquid [10]. Here we investigate a liquid/liquid boundary by studying the capillary driven levelling of a thin liquid bilayer film. The levelling is driven by the surface tension, γ , of the liquid. Curvature at the surface of a liquid results in a Laplace pressure and induces flow in order to reduce the excess surface area, thereby reducing the surface energy associated with the system. The flow is mediated by the viscosity of the liquid, η . With well-known initial conditions, capillary driven levelling can be used to study the glass transition temperature of polymers [11, 12], confinement effects [13] and nanorheology of polymeric films [14] to name just a few.

Previous work in nanorheology of thin films has shown that boundary conditions dictate the resulting flow of liquid films [15–17]. A variety of geometries have been previously studied [18–20], but here we employ the stepped film geometry: the initial surface perturbation can be described as a Heaviside step function where the height profile varies along the x direction from one thickness to another and is invariant in the orthogonal in-plane direction. The height profile can then be described as a function of the horizontal position and time, $h = h(x, t)$. In the simplest case a thin liquid film on a solid substrate has a no-slip boundary condition at the solid-liquid interface and a no-stress boundary condition at the liquid/air interface. Using the lubrication approximation and Stokes flow, the interface profile follows the standard thin film equation [1] and the governing flow is a parabolic Poiseuille flow. The thin film equation admits a self-similar solution with the rescaling variable, $x/t^{1/4}$ [21, 22]. As a result, the levelling of any film with the same boundary conditions will approach the same self-similar attractor regardless of the initial geometry of the perturbation [23, 24]. A modification of the no-slip boundary condition of a liquid film supported on a substrate arises in the case of a freestanding film. Such a liquid film has no-stress boundary conditions at both interfaces

* These authors contributed equally to this work

† dalnoki@mcmaster.ca

and does not support shear. In that case the excess surface energy is dissipated through elongational flow, as found in soap films [25]. Using a long-wave approximation, the flow profile is consistent with plug flow. The governing equation for the interface profile, $h(x, t)$, follows a system of coupled partial differential equations [26] which admits a self-similar solution with the rescaling variable, $x/t^{1/2}$ [27]. Lastly, we note that freestanding film models follow the same equation as that of a supported film in the case of a infinite slip length (no shear stress is supported at the supported interface) [16].

For a liquid thin film on a liquid substrate, the flow profile is less clear and depends on the viscosity ratio between the two substrates, as well as the relative surface and interfacial tensions. One can speculate that the levelling of a film on a more viscous liquid will tend to that of a film on a solid substrate. The opposite case of the levelling of a film on a lower viscosity fluid is not trivial and it is the primary focus of this paper. In addition, the presence of slip at the liquid/liquid interface may affect the levelling dynamics. Here, we employ experiments with thin immiscible bilayer films and theory to investigate the hydrodynamic flow in such a geometry. We demonstrate that there is a power law crossover between the Poiseuille and plug flow regimes discussed above that are tuneable with the relative viscosity ratio.

II. METHODS

A. Experimental

The sample preparation follows closely a modified version of that described in [28] Thin polymer films were prepared by spin coating either polystyrene (PS) or poly(methyl methacrylate) (PMMA) from solution in toluene (Fisher Chemical, Optima). PS and PMMA were chosen for their immiscibility with each other. The PS and PMMA films were spincoated onto 1×1 cm silicon wafers (University Wafer) and freshly cleaved mica sheets (Ted Pella, Inc.) respectively. The PMMA molecular weight was $M_w = 56$ kg/mol (Polymer Source, Inc., polydispersity index ≤ 1.08). The molecular weights of the PS were 53.3, 106, 183, and 758.9 kg/mol (Polymer Source, Inc. and Scientific Polymer Products, Inc., polydispersity index ≤ 1.06). After spincoating, all films were annealed at 150°C for 10 minutes to remove any remaining solvent and to relax the polymer chains. The films of PMMA were floated from the mica surface onto a bath of ultra-pure water ($18.6 \text{ M}\Omega \text{ cm}$). A full section of the PMMA was lifted off the water surface onto the PS coated silicon to create a bilayer film supported on the Si substrate: PMMA/PS/Si. The molecular weight of the PMMA is low enough so that the polymer chains are not highly entangled, such a film easily fractures upon perturbation on the surface of water and results in clean straight edges [18]. A second film of PMMA was fractured and transferred onto the sample, where the sharp fracture edge create a PMMA step. Figure 1(a) shows a schematic of the sample, with a stepped film of PMMA sitting atop a PS film. For all of the experiments, the three layers, h_{PS} , $h_{\text{PMMA-u}}$ and $h_{\text{PMMA-l}}$, were of nominally the same thickness and confirmed to be within 10% of each other using ellipsometry (Accurion, EP3).

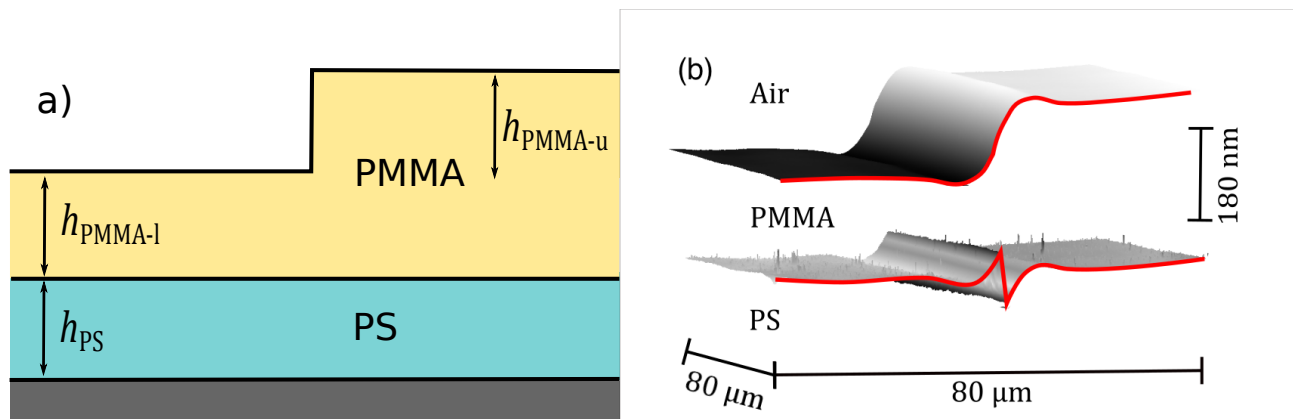


FIG. 1. (a) A schematic of the as-prepared sample, where the three layers are indicated with the given material. $h_{\text{PMMA-u}}$ indicates the thickness of the upper portion of the step, $h_{\text{PMMA-l}}$ indicates the thickness of the lower portion of the step, and h_{PS} indicates the thickness of the underlying liquid film. (b) Atomic force microscopy profiles for the liquid/air interface and the liquid/liquid interface. The two scans are artificially shifted in the vertical direction to simulate the actual geometry of the sample.

To examine the progression of the step with time, the samples were heated above the glass transition temperature of both polymers ($\sim 100^\circ\text{C}$) with a temperature controlled stage (Linkam). The samples were heated for a period of time to enable flow before being quenched back into the glassy state at room temperature. Surface profiles of the liquid/air interface were taken using atomic force microscopy (AFM, Bruker). For some experiments, the liquid/liquid interface was exposed by dissolving the top PMMA layer with a selective solvent ($\sim 66\%$ acetic acid and $\sim 33\%$ ultra-pure water). Figure 1(b) shows an example of an AFM scan of the liquid/air and liquid/liquid interface taken at the same location on the sample. The geometry of the sample is visualized here by vertically shifting the AFM scans by the original layer thickness.

B. Theory

We have a system with two liquid films atop of a rigid substrate as pictured in Fig. 1(a). A Cartesian coordinate system (x, y, z) is used, the vertical coordinate is denoted by z and the out of plane direction is denoted by y . We assume that the system is infinite in the x - and y - direction and that both liquids are Newtonian incompressible fluids. With symmetry arguments the out-of-plane direction, y is invariant with time. The typical length scale of the experiment (film thickness on the order of 100 nm) is well below the capillary length, thus gravitational effects can be neglected in comparison to capillary forces. The flows correspond to low Reynolds numbers so that inertial effects can be neglected. Lastly, the film thicknesses are chosen large enough such that van der Waals interactions result in a pressure that is weak in comparison to the Laplace pressure [21].

The velocity fields, pressure fields, and viscosity of the two fluids are denoted $\vec{u}_i = (u_i, 0, w_i)$, p_i and η_i with $i \in [1, 2]$ being the layer number. Layer 1 is the PS film, and layer 2 is the PMMA step. The surface tension of the top liquid is defined as γ_2 and the liquid/liquid interfacial tension is denoted γ_1 . Two dimensionless numbers arise from these definitions: the surface tension and viscosity ratios $\gamma = \gamma_1/\gamma_2$ and $\eta = \eta_1/\eta_2$. The molecular weight of the bottom layer is varied in the different experiments which results in a massive change in the viscosity ratio (3 orders of magnitude $\eta = 0.0005$ to 1). The liquid/liquid interfacial tension does not vary with the molecular weight of the polymers and will taken to be $\gamma = 0.053$ [29]. Within the lubrication approximation there is continuity of the tangential stress across the liquid/liquid interface, thus $\eta_1 \frac{\partial u_1}{\partial z} = \eta_2 \frac{\partial u_2}{\partial z}$ [17]. For a system with two liquids and where $\eta \ll 1$, this relationship should be $\frac{\partial u_2}{\partial z} = 0$ to leading order. Together with a no-stress boundary condition at the liquid/air interface, this boundary condition is consistent with plug flow in the top layer. There is a correction due to the tangential stress of the bottom layer at the next leading order, this rescales the viscosity ratio [30].

Dimensionless variables are denoted with a hat as they are introduced here, and the hat will be dropped for the remainder of this paper and dimensionless variables are assumed

$$u_i = U \hat{u}_i, \quad w_i = W \hat{w}_i = U \epsilon \hat{w}_i, \quad x = L \hat{x}, \quad z = H \hat{z}, \quad p_i = P \hat{p}_i, \quad t = \frac{L}{U} \hat{t}, \quad h_i = H \hat{h}_i, \quad \epsilon = \frac{H}{L}, \quad (1)$$

where: ϵ is the ratio between the typical vertical scale H (fixed by the thickness of the layers) and the horizontal length scale L , $P = \frac{\gamma_2 H}{L^2}$ is the typical pressure scale set by the Laplace pressure, $U = \frac{\gamma_2 H}{\eta_2 L}$ is the characteristic velocity which is chosen such that the leading order equation for the top layer is compatible with plug flow. The pressures are the Laplace pressures associated with each interface, where $p_2 = \gamma_2 (\partial^2 h_2 / \partial x^2)$ and $p_1 = p_2 - \gamma_1 (\partial^2 h_1 / \partial x^2)$. As indicated above, we rescale the viscosity ratio as $\eta = \epsilon^2 \hat{\eta}$. The resulting profiles follow a set of non-linear partial differential equations, and the calculation details may be found in Appendix A. The governing equations are

$$\partial_t (h_2 - h_1) = -[(h_2 - h_1)u_2]', \quad (2a)$$

$$\partial_t h_1 = - \left[(\gamma_2 h_2''' + \gamma_1 h_1''') \frac{h_1^3}{12\eta_1} + \frac{h_1 u_2}{2} \right]' = - \left(-p_1' \frac{h_1^3}{12\eta_1} + \frac{h_1 u_2}{2} \right)', \quad (2b)$$

$$\gamma_2 h_2''' (h_2 - h_1) + (\gamma_2 h_2''' + \gamma_1 h_1''') \frac{h_1}{2} + 4\eta_2 [u_2' (h_2 - h_1)]' - \eta_1 \frac{u_2}{h_1} = 0, \quad (2c)$$

where the prime indicates a derivative with respect to x . Notably, equation 2c has the same form as the tangential stress balance for a single liquid film on a solid with large slip length [16]. The apparent slip length that comes from this model is in terms of the geometry of the system, $b_{\text{slip}} = h_1 \eta_2 / \eta_1$ [30], which can be large as the viscosity of two polymer melts can vary greatly.

The height of the two interfaces can be expressed as perturbations from the mean thickness of the fluid later, $h_1(x, t) = \bar{h}_1 + \delta h_1(x, t)$ and $h_2 = \bar{h}_1 + \bar{h}_2 + \delta h_2(x, t)$, where \bar{h}_i denotes the mean thickness of the fluid layer at rest. For clarity, the mean thicknesses can be defined in terms of the experimental thicknesses: $\bar{h}_1 = h_{\text{PS}}$ and $\bar{h}_2 = h_{\text{PMMA-1}} + \frac{1}{2}h_{\text{PMMA-u}}$ defined. In order to proceed analytically, only the linear terms are considered since $\delta h_i \ll \bar{h}_i$. This assumption is not valid with respect to the experiment because the step height is of the same order of magnitude as the thickness of the fluid. Nevertheless, the essential physics is contained in the linear solution and captures the experimental results. The Fourier transform \tilde{f} of a function $f(x)$ is $\tilde{f}(k) = \frac{1}{\sqrt{2\pi}} \int dx f(x) \exp(ikx)$, and we find that the Fourier transform of the interface profile can be written as

$$\frac{\partial \delta \tilde{h}_i}{\partial t} = s_{i,j}(k) \delta \tilde{h}_j, \quad (3)$$

with $s_{i,j}$ representing the growth rate associated with the mode, k . The growth rate is defined in Appendix A. The general solution of this set of equations is

$$\delta \tilde{h}_1 = \alpha \exp \lambda_1 t + \beta \exp \lambda_2 t, \quad (4a)$$

$$\delta \tilde{h}_2 = \alpha K_1 \exp \lambda_1 t + \beta K_2 \exp \lambda_2 t. \quad (4b)$$

The eigenvalues and eigenvectors of the matrix \bar{s} are (λ_1, λ_2) and $(1, K_1), (1, K_2)$, respectively. The two coefficients α and β can be found using the initial conditions: $\delta h_1(x, t = 0) = 0$, and $\delta h_2(x, t = 0) = \frac{1}{2} h_{\text{PMMA}}[\Theta(x) - 1/2]$, where Θ denotes the Heaviside function (i.e. $\Theta(x > 0) = 1, \Theta(x < 0) = 0$).

To consider the validity of the model explained above, a second model was developed that does not assume flow profiles in the respective layers and takes into account all the terms of the Stokes equation. This Stokes model is detailed in Appendix C, but it is important to note that it assumes the step height is a perturbation in relation to the thickness of the film. This model exhibits a similar governing equation to Eq. (3), with the exception of the growth rates $s_{i,j}^S$, which are much more complicated functions of k . Excellent agreement between the solutions of both models is found on the experimental time scale, which in turn confirms the pertinence of the model developed in this section (see Fig. 5).

III. RESULTS AND DISCUSSION

Figure 2(a) shows the liquid/air interface and the liquid/liquid interface at different stages of evolution.

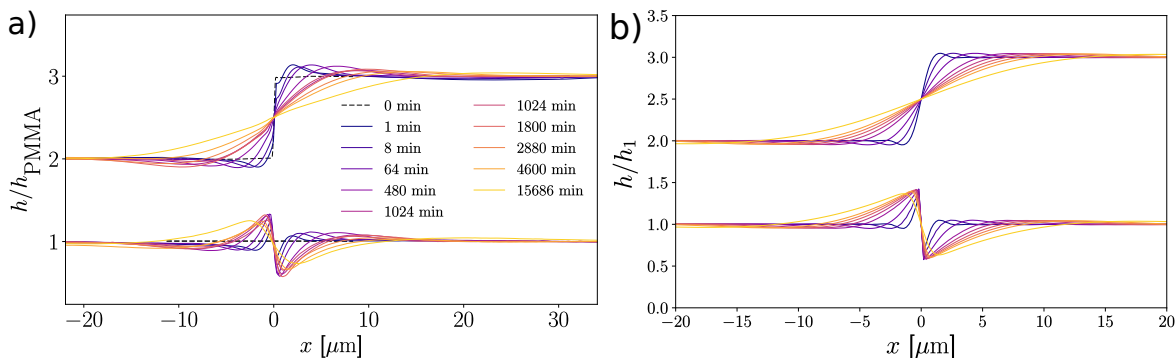


FIG. 2. a) Experimental profiles of the liquid/air and liquid/liquid interfaces of a PMMA step on PS ($M_w = 53.3$ kg/mol) during levelling at $T = 150$ °C. The samples were fabricated to have $h_{\text{PS}} = h_{\text{PMMA-1}} = h_{\text{PS-u}} = 180$ nm. The top liquid was removed with a selective solvent to expose the liquid/liquid interface. b) Theoretical profiles calculated from the asymptotic model. The times, physical properties and geometry of the calculated step have been inputted to match the experimental conditions in frame a).

In these profiles, the PS has a $M_w = 53$ kg/mol and the samples were annealed at 150 °C. The liquid/air interface develops a “bump” on the upper side of the step with positive curvature and a “dip” on the lower side with negative

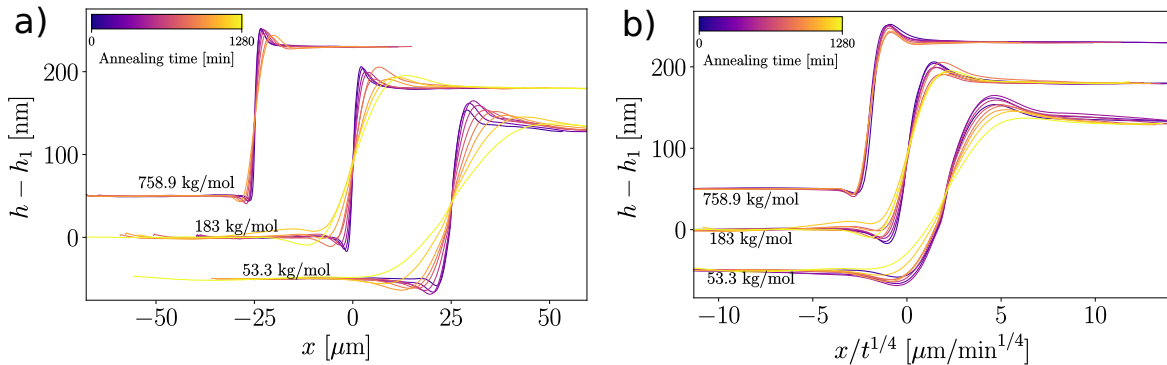


FIG. 3. (a) Height of three PMMA steps as a function of horizontal position and time ($0 < t < 1280$ min). The steps are sitting on thin PS films of varying molecular weights, as indicated, and annealed at 165°C . (b) Heights of the three PMMA steps as shown in (a), but with the horizontal axis rescaled with an annealing time power law, $t^{1/4}$. For both sections, the 53.3 and 758.9 kg/mol data has been shifted horizontally and vertically for clarity.

curvature. With increased annealing time, the bump and dip spread apart across the substrate as the step levels. As discussed in previous works [22], the bump and dip develop to alleviate the large gradients in Laplace pressure which originates due to the highly curved corners of the original step geometry. At early annealing times, $t < 8$ min, there is a non-smooth feature near the center of the step that is a remnant of the initial corner of the step.

The liquid/liquid interface deforms significantly in response to the Laplace pressure from the step above. Remarkably, the feature initially grows before decreasing in height – this implies that while the energy associated with the liquid/air interface decreases, it does so at the cost of an increasing surface energy at the liquid/liquid interface. On either side of the deformation are shapes that mimic the bump and dip of the liquid/air interface. The large deformation of the liquid/liquid interface, relative to the layer thickness, can be explained by considering two physical properties of the system: the viscosity ratio between the PMMA and the PS, and the ratio between the surface tension of the liquid/air interface and the interfacial tension of the liquid/liquid interface. The interfacial tension plays a crucial role in the magnitude of the energy required to deform a surface, for this system the PMMA-air interfacial tension, $\gamma_{PMMA-air} = 31.22$ dyn/cm, is much larger than that of the PS-PMMA interface, $\gamma_{PS-PMMA} = 1.65$ dyn/cm [29]. Since the interfacial tension ratio $\gamma = \gamma_{PMMA-air}/\gamma_{PS-PMMA}$ is large, the lower interface is less energetically costly to deform than the liquid/air interface. The liquid/liquid interface then follows the shape of the liquid/air interface with relatively little energetic cost, and thus the deformation of the liquid/liquid interface can be inferred from the shape of the liquid/air interface. Figure 2 shows a comparison of the levelling profiles, where Fig 2(a) shows the profiles that were obtained experimentally and Fig 2(b) contains the profiles generated with the theoretical model with matching physical parameters to the experimental data. The model clearly captures the essential features that are observed in the experiment.

The effect of the viscosity ratio between the top and bottom polymers was examined by varying the molecular weight of the PS layer. Figure 3(a) shows the profiles of PMMA steps on top of films of three different PS molecular weights, 53.3, 183, and 758.9 kg/mol. The viscosity ratios between PS and PMMA were measured independently using the same capillary levelling technique outlined in previous works [28] i.e. stepped films were prepared from a single polymer (PS or PMMA) and the capillary velocity was determined at the same temperature at which all bilayer experiments were carried out. The viscosity ratios, $\eta = \eta_{PS}/\eta_{PMMA}$, in order of increasing PS molecular weight, are 6×10^{-5} , 1×10^{-2} , and 1. For the profiles in Fig. 2(a) and Fig. 3(a), the viscosity of the top film is always larger or equal to the viscosity of the bottom film. The flow of the system is driven by gradients in Laplace pressure along the step. The pressure is continuous through the PMMA layer and is transferred to the PS layer below, thereby inducing flow in the PS layer. The deformation of the bottom layer is the result of flow in the less viscous medium in response to the step, which occurs more quickly than the more viscous top layer. It is immediately clear from Fig. 3(a) that for samples having identical annealing times and geometry, the lower the viscosity of the underlying PS film, the faster the levelling progresses.

The profiles can be rescaled by a temporal power law to determine if the profiles are self-similar [21, 22, 28]. As discussed above, for Poiseuille flow, the surface profiles change with a power law of $t^{1/4}$, while for plug flow $t^{1/2}$ evolution of the profiles is found. Figure 3(b) shows the same profiles as in Fig. 3(a) with the horizontal axis rescaled as expected for a Poiseuille based flow. For the smallest viscosity ratio (PS $M_w = 758.9$ kg/mol), the profiles collapse well with $t^{1/4}$. However, for the two larger viscosity ratios, there is no simple collapse, which suggests that there is

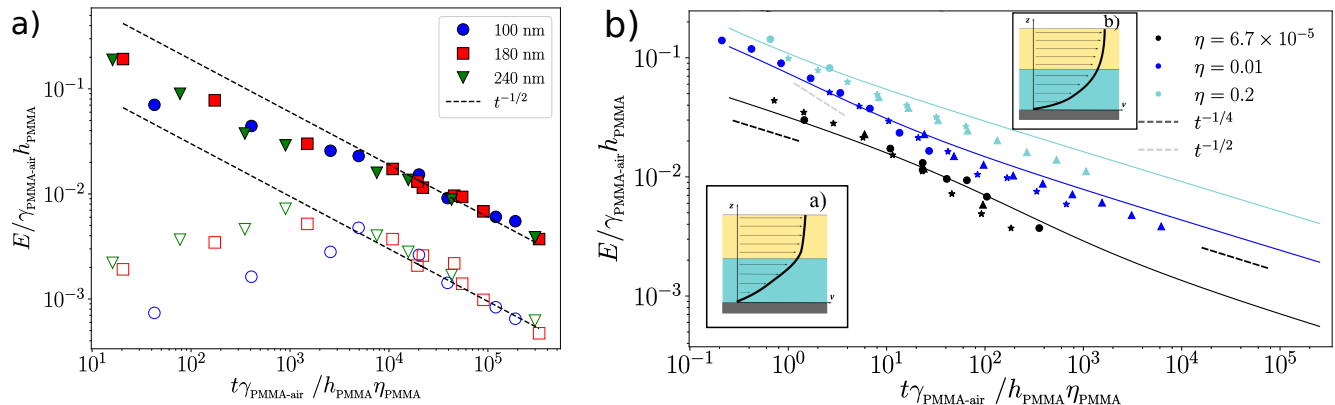


FIG. 4. (a) Excess capillary energy of the liquid/air interface (filled) and liquid/liquid interface (unfilled) for a PMMA ($M_w = 56$ kg/mol) step on a thin film of PS ($M_w = 53.3$ kg/mol) annealed at 150°C . The $t^{1/4}$ line is present to guide the reader for late time behaviour. The energy has been normalized by the initial capillary energy of the system. (b) Excess capillary energy of the liquid/air interface for a PMMA ($M_w = 56$ kg/mol, height = 180 nm) step on thin films of PS ($M_w = 53.3, 183,$ and 758.9 kg/mol) annealed above T_g . Samples were annealed at 150°C (\circ), 165°C (\star) and 180°C (\triangle) and shifted relative to the 150°C data using time-temperature superposition. The energy has been normalized by the initial capillary energy of the system. Inset a) is a schematic of flow profiles pertaining to a bilayer system with a small viscosity ratio. Inset b) is a schematic of flow profiles pertaining to a bilayer system with a viscosity ratio of 1.

no self-similar solution scaling with $t^{1/4}$ for the experimental time scale studied. In order to investigate the temporal evolution in more detail, we follow the approach by McGraw *et al.* [21] and consider the evolution of the surface energy of the system as this is a global observable linked to the step evolution.

The surface energy or capillary energy, E , of a fluid surface is proportional to the surface/interfacial tension γ_i of the interface, i . Furthermore, the capillary energy is proportional to the excess area of the surface, S , compared to a flat surface, S_o : $E = \gamma_i \int (dS - dS_o)$. Due to the large interfacial tension ratio, γ , the energetic contribution of the liquid/liquid interface is negligible in comparison to the liquid/air. Since the liquid/liquid interface has an energetic cost that is so much less than that of the liquid/air interface, we can approximate the change in energy as a function of time simply by the change in surface area of the liquid/air interface multiplied by the surface tension of PMMA. Figure 4(a) shows the capillary energy of the liquid/air and liquid/liquid interfaces for PS ($M_w = 53.3$ kg/mol) annealed at 150°C obtained by integrating the experimentally obtained surface profile. For these samples, the layer thickness, h_{PMMA} , was 100, 180 or 240 nm. To account for the different initial excess surface areas resulting from the different step heights, the energy is normalized by the initial excess surface energy, $E_{\text{init}} = \gamma_{\text{PMMA/air}} h_{\text{PMMA}}$. As expected, the energy contribution of the liquid/liquid interface is measured to be about an order of magnitude less than that of the liquid/air interface. For this reason, in what is to follow we approximate the total energy of the system by following only the liquid/air surface. We note that the reason for doing so is that in order to track the liquid/liquid interface, each measured profile requires rinsing away the top surface thus many equivalent samples are needed in order to generate the data shown in Fig. 4(a). In contrast, having validated that the liquid/liquid interface does not significantly contribute to the overall energy, one can prepare a single sample and follow its liquid/air profile evolution.

Figure 4(b) shows the liquid/air interface evolution for the three different viscosity ratios. The experimental data is overlaid with the energy obtained from the theoretical model to show that qualitative agreement is found between the theory and experiment. To understand why the different viscosity ratios demonstrate different time dependencies, we must consider the mechanism by which the energy is dissipated. As these films are thin and body forces may be neglected, we can consider only viscous dissipation. The viscous energy dissipation depends on the flow profile of the liquid. Using conservation of energy, the capillary energy must be relieved through viscous dissipation. Taking the model developed in the previous section, we write the conservation of energy as

$$\partial_t E = - \underbrace{\int dx 4\eta_2 (h_2 - h_1) u_2^2}_{\text{Plug}} - \underbrace{\int dx \frac{p_1^2 h_1^3}{12\eta_1}}_{\text{Poiseuille-like}} - \underbrace{\int dx \eta_1 \frac{u_2^2}{h_1}}_{\text{Couette-like}}. \quad (5)$$

Here the first term has a velocity profile that is invariant in z corresponding to plug flow, the second term has a

parabolic velocity profile or Poiseuille-like flow, whereas the last term corresponds to a linear variation in the velocity profile as seen in a simple shear geometry or Couette-like flow.

According to the model outlined in the theoretical section, a small viscosity ratio will result in plug flow of the top film, with Couette-like flow in the bottom film. A schematic of this configuration is shown in inset (a) of Fig. 4(b). Conversely, for viscosity ratio ~ 1 , there is no regime where plug flow is present. The system rapidly converges on the asymptotic solution of Poiseuille on Poiseuille flow, a schematic of this is shown in inset (b) of Fig. 4(b). Therefore, the energy directly follows $t^{1/4}$ scaling. This explains the perfect collapse of the profiles in Fig. 3(b) for PS $M_w = 758.9$ kg/mol with $t^{-1/4}$ rescaling.

As the viscosity ratio increases in magnitude, the influence of the top layer plug flow decreases. At early times, this mechanism for viscous dissipation reduces the energy the most rapidly. Plug-like flow is sustained until the driving force has diminished sufficiently and Couette-like flow dominates. One can think of this as an analogy to a stepped film on a substrate with slip, where the bottom film acts as a lubrication layer for the top film. Then the slip length is given as $b = h_1 \eta_2 / \eta_1$. To continue the analogy, Couette flow can then be simplified as a frictional component while the top film is slipping along the ‘substrate’ (the bottom film). For small viscosity ratios the majority of the flow is dissipated through Poiseuille and plug flow, before changing to Couette flow (or what can be thought of as the top film slipping along a surface). The change from Poiseuille and plug flow to Couette flow occurs earlier for larger viscosity ratios, as the frictional Couette term increases with increasing bottom film viscosity.

IV. CONCLUSION

In this paper, we examined the effect of a liquid boundary on the flow of a nanoscale film. We prepared a stepped thin polymer film that was layered onto a second immiscible polymer film supported on a solid substrate. The films were observed to flow towards an equilibrium flat film, however, the liquid/liquid interface was found to substantially deform in the process. In the prepared samples, the viscosity of the bottom liquid was lower than the liquid step. We have shown that the viscosity ratio between the two liquids has a major impact on the resulting viscous flow. Unlike viscous flow of thin films on solid substrates or freestanding films, the surface profiles do not exhibit self-similar leveling profiles as previously observed [27, 28]. Rather, we see a rich crossover as energy is dissipated by a combination of three different flow mechanisms: parabolic Poiseuille flow, linear Couette flow, and invariant plug flow. We have constructed a model to consider the energy dissipation of the capillary energy associated with the step, which is motivated by previous works [17, 21, 30]. The dominant viscous dissipation mechanism was found to cross-over from plug and Poiseuille flow in the top film to Couette flow in the bottom film at late times. The time of cross-over depends on the viscosity ratio between the top and the bottom liquids. The experimentally measured energy dissipation is in qualitative agreement with that obtained in the model. Lastly, we have presented the data in the context of a hydrodynamic model using a linearized set of Stokes equations that confirms the asymptotic model.

ACKNOWLEDGMENTS

Appendix A: Asymptotic flow

1. Model

This appendix expands upon the calculation of the asymptotic model discussed in the theoretical section. The governing equations for the model are the Stokes equations for both liquid films

$$0 = -\epsilon^2 \partial_x p_2 + \epsilon^2 \partial_x^2 u_2 + \partial_z^2 u_2, \quad (\text{A1a})$$

$$0 = -\partial_z p_2 + \epsilon^2 \partial_x^2 w_2 + \partial_z^2 w_2, \quad (\text{A1b})$$

$$\partial_x u_2 + \partial_z w_2 = 0, \quad (\text{A1c})$$

$$0 = -\partial_x p_1 + \eta[\epsilon^2 \partial_x^2 u_2 + \partial_z^2 u_1], \quad (\text{A1d})$$

$$0 = -\partial_z p_1 + \eta[\epsilon^4 \partial_x^2 w_1 + \epsilon^2 \partial_z^2 w_1], \quad (\text{A1e})$$

$$\partial_x u_1 + \partial_z w_1 = 0. \quad (\text{A1f})$$

At the free interface, the boundary conditions are due to the stress balance and the kinematic condition

$$p_2 + \frac{\partial_x^2 h_2}{(1 + \epsilon^2(\partial_x h_2)^2)^{3/2}} = 2 \frac{(\partial_z w_2 [1 - \epsilon^2(\partial_x h_2)^2] - (\partial_z u_2 + \epsilon^2 \partial_x w_2) \partial_x h_2)}{1 + \epsilon^2(\partial_x h_2)^2}, \quad z = h_2, \quad (\text{A2a})$$

$$(\partial_z u_2 + \epsilon^2 \partial_x w_2)(1 - \epsilon^2(\partial_x h_2)^2) = 4\epsilon^2 \partial_x u_2 \partial_x h_2, \quad z = h_2, \quad (\text{A2b})$$

$$\partial_t h_2 = w_2 - u_2 \partial_x h_2, \quad z = h_2. \quad (\text{A2c})$$

The boundary conditions at the liquid/liquid interface are the stress balance and the kinematic condition. Furthermore, we assume that there is no-slip at the interface due to the interpenetrability of the two polymers,

$$p_1 - p_2 + \gamma \frac{\partial_x^2 h_1}{(1 + \epsilon^2(\partial_x h_1)^2)^{3/2}} = 2 \frac{(\partial_z [\eta \epsilon^2 w_1 - w_2] [1 - \epsilon^2(\partial_x h_1)^2] - (\partial_z [\eta \epsilon^2 u_1 - u_2] + \epsilon^2 \partial_x [\eta \epsilon^2 w_1 - w_2]) \partial_x h_1)}{1 + \epsilon^2(\partial_x h_1)^2}, \quad z = h_1 \quad (\text{A3a})$$

$$(\partial_z [\eta \epsilon^2 u_1 - u_2] + \epsilon^2 \partial_x [\eta \epsilon^2 w_1 - w_2]) (1 - \epsilon^2(\partial_x h_1)^2) = 4\epsilon^2 \partial_x [\eta \epsilon^2 u_1 - u_2] \partial_x h_1, \quad z = h_1 \quad (\text{A3b})$$

$$\partial_t h_1 = w_1 - \partial_x h_1, \quad z = h_1 \quad (\text{A3c})$$

$$w_2 - w_1 = [u_2 - u_1] \partial_x h_1, \quad z = h_1 \quad (\text{A3d})$$

$$u_2 - u_1 + \epsilon^2 [w_2 - w_1] \partial_x h_1 = v_{\text{slip}} = 0, \quad z = h_1. \quad (\text{A3e})$$

At the solid interface, we assume a no-slip boundary condition,

$$u_1 = w_1 = 0, \quad z = 0. \quad (\text{A4})$$

We consider the flow in the top film as a perturbation from a first order system

$$(u_2, w_2, p_2) = \left(u_2^{(0)}, w_2^{(0)}, p_2^{(0)} \right) + \epsilon^2 \left(u_2^{(1)}, w_2^{(1)}, p_2^{(1)} \right). \quad (\text{A5})$$

After some algebra, the leading order flow of the system can be described as

$$\partial_z u_2^{(0)}(x, z, t) = 0 \quad \rightarrow \quad u_2^{(0)}(x, z, t) = u_2(x, t), \quad (\text{A6a})$$

$$w_2^{(0)}(x, z, t) = -(z - h_1) \partial_x u_2 + w_1(z = h_1), \quad (\text{A6b})$$

$$p_2^{(0)}(x, z, t) = -2\partial_x u_2 - \partial_x^2 h_2, \quad (\text{A6c})$$

$$\partial_z p_1(x, z, t) = 0, \quad (\text{A6d})$$

$$u_1(x, z, t) = -\frac{1}{2\eta} \partial_x p_1 (z^2 - zh_1) + u_2(x, t) \frac{z}{h_1}. \quad (\text{A6e})$$

The in-plane component of the flow is described by set of coupled non-linear equations. To consider the time dependent flow as a function of height instead, we impose the kinematic condition. This results in the first governing equation discussed in the main text of this paper, Eq. (2a),

$$\partial_t(h_2 - h_1) = -([h_2 - h_1]u_2)', \quad (\text{A7})$$

where a prime denotes the derivative with respect to x . The volume conservation of the bottom liquid gives the second governing equation, Eq. (2b),

$$\partial_t h_1 = - \left(-p'_1 \frac{h_1^3}{12\eta_1} + \frac{h_1 u_2}{2} \right)' = - \left((\gamma_2 h_2''' + \gamma_1 h_1''') \frac{h_1^3}{12\eta_1} + \frac{h_1 u_2}{2} \right)'. \quad (\text{A8})$$

The final equation that relates u_2 to the other variables can be found by integrating the horizontal component of the Stokes equation with respect to z at the next leading order

$$\partial_z^2 u_2^{(1)} + \partial_x^2 u_2^{(0)} = \partial_x p_2^{(0)} \quad \rightarrow \quad \partial_z u_2^{(1)}(z = h_2) - \partial_z u_2^{(1)}(z = h_1) = \left(\partial_x p_2^{(0)} - \partial_x^2 u_2 \right) (h_2 - h_1). \quad (\text{A9})$$

We find the last governing equation, Eq. (2c), by inserting the two tangential stress balances, Eq. (A2b) and Eq. (A3b), at leading order into the previous equation,

$$h_2'''(h_2 - h_1) + (h_2''' + \gamma h_1''')h_1/2 + 4(u_2'(h_2 - h_1))' - \eta \frac{u_2}{h_1} = 0 \quad (\text{A10})$$

2. Growth rates

The rate of change for the profiles are found by substituting a form of solution and expanding at the leading order in δh_i .

$$s_{1,1}(k) = -\gamma_1 k^4 \left(\frac{\bar{h}_1^3}{12\eta_1} + \frac{\bar{h}_1^3}{4(\eta_1 + 4\eta_2 k^2 \bar{h}_1 \bar{h}_2)} \right), \quad (\text{A11a})$$

$$s_{1,2}(k) = -\gamma_2 k^4 \left(\frac{\bar{h}_1^3}{12\eta_1} + \frac{\bar{h}_1^2 \bar{h}_2 (1 + \frac{\bar{h}_1}{2\bar{h}_2})}{2(\eta_1 + 4\eta_2 k^2 \bar{h}_1 \bar{h}_2)} \right), \quad (\text{A11b})$$

$$s_{2,1}(k) = -\gamma_1 k^4 \left(\frac{\bar{h}_1^3}{12\eta_1} + \frac{\bar{h}_1^2 \bar{h}_2 (1 + \frac{\bar{h}_1}{2\bar{h}_2})}{2(\eta_1 + 4\eta_2 k^2 \bar{h}_1 \bar{h}_2)} \right), \quad (\text{A11c})$$

$$s_{2,2}(k) = -\gamma_2 k^4 \left(\frac{\bar{h}_1^3}{12\eta_1} + \frac{\bar{h}_1 \bar{h}_2^2 (1 + \frac{\bar{h}_1}{2\bar{h}_2})^2}{(\eta_1 + 4\eta_2 k^2 \bar{h}_1 \bar{h}_2)} \right). \quad (\text{A11d})$$

Appendix B: Energy balance

In this section, we derive the energy balance in Eq. (5). In the limit of small slope, the capillary energy of the two interfaces (per unit of out of plane length)

$$E_2 = \frac{\gamma_2}{2} \int dx h_2'(x)^2, \quad (\text{B1a})$$

$$E_1 = \frac{\gamma_1}{2} \int dx h_1'(x)^2. \quad (\text{B1b})$$

We can derive these quantities with respect to time

$$\partial_t E_2 = \gamma_2 \int dx h_2' \partial_t h_2' = -\gamma_2 \int dx h_2'' \partial_t h_2, \quad (\text{B2a})$$

$$\partial_t E_1 = \gamma_1 \int dx h_1' \partial_t h_1' = -\gamma_1 \int dx h_1'' \partial_t h_1. \quad (\text{B2b})$$

The second equality is obtained using integration by parts. We can then use the relations Eq.(2a) and Eq.(2b)

$$\partial_t E_2 = -\gamma_2 \int dx h_2'' (\partial_t h_1 - [(h_2 - h_1)u_2]') = -\gamma_2 \int dx h_2'' \left(- \left[-p_1' \frac{h_1^3}{12\eta_1} + \frac{h_1 u_2}{2} \right]' - [(h_2 - h_1)u_2]' \right), \quad (\text{B3a})$$

$$\partial_t E_1 = \gamma_1 \int dx h_1'' \left(-p_1' \frac{h_1^3}{12\eta_1} + \frac{h_1 u_2}{2} \right)'. \quad (\text{B3b})$$

We then use integration by parts again

$$\partial_t E_2 = \gamma_2 \int dx h_2''' \left(- \left[-p_1' \frac{h_1^3}{12\eta_1} + \frac{h_1 u_2}{2} \right] - [(h_2 - h_1)u_2] \right), \quad (\text{B4a})$$

$$\partial_t E_1 = -\gamma_1 \int dx h_1''' \left(-p_1' \frac{h_1^3}{12\eta_1} + \frac{h_1 u_2}{2} \right). \quad (\text{B4b})$$

To consider the total energy of the system, we can sum the two capillary energies, $E = E_1 + E_2$, associated with the two interfaces

$$\partial_t E = - \int dx [\gamma_2 h_2''' (h_2 - h_1)] u_2 + \int dx p_1' \left(-p_1' \frac{h_1^3}{12\eta_1} + \frac{h_1 u_2}{2} \right). \quad (\text{B5})$$

We can then use Eq.(2c) to replace the term in square brackets

$$\partial_t E = - \int dx \left[-p_1' h_1 / 2 - 4\eta_2 (u_2' (h_2 - h_1)' + \eta_1 \frac{u_2}{h_1}) \right] u_2 + \int dx p_1' \left(-p_1' \frac{h_1^3}{12\eta_1} + \frac{h_1 u_2}{2} \right). \quad (\text{B6})$$

This can be further simplified and after another integration by parts using $u_2' (h_2 - h_1)'$, it yields to

$$\partial_t E = - \int dx 4\eta_2 (h_2 - h_1) u_2'^2 - \int dx \eta_1 \frac{u_2^2}{h_1} - \int dx \frac{p_1'^2 h_1^3}{12\eta_1}. \quad (\text{B7})$$

The capillary energy lost per unit time can be written as the sum of three different methods of viscous dissipation. The first term corresponds to the dissipation that occurs through elongational viscosity in the top fluid. This is consistent with plug flow. The two other terms are shear terms in the bottom film associated with Couette and Poiseuille flow.

Appendix C: Stokes model

To remove any assumptions associated with flow type and the resulting scaling of the energy, we derive a model from the Stokes equations [31, 32]. The stream function of the hydrodynamic flow, ψ_i , ($i = 1, 2$ is the layer number as described in Appendix A)

$$u_i = -\partial_z \psi_i, \quad (\text{C1a})$$

$$w_i = \partial_x \psi_i. \quad (\text{C1b})$$

The velocity field verifies the Stokes equations. This in turn implies that the stream functions are solutions of the biharmonic equation.

$$(\partial_x^4 + 2\partial_x^2 \partial_z^2 + \partial_z^4) \psi_i = 0. \quad (\text{C2})$$

We take the Fourier transform of the biharmonic equation (denoted as $\tilde{\psi}$) with respect to the x -coordinate (defined in the main text) with results in a fourth order ordinary differential equation

$$\left(\frac{d}{dz} \right)^4 \tilde{\psi}_i - \left(\frac{d}{dz} \right)^2 k^2 \tilde{\psi}_i + k^4 \tilde{\psi}_i = 0. \quad (\text{C3})$$

The general solution verifies the fourth order ordinary differential equation

$$\tilde{\psi}_i(k, z) = A_i(k) \cosh(kz) + B_i(k) \sinh(kz) + C_i(k)z \cosh(kz) + D_i(k)z \sinh(kz). \quad (\text{C4})$$

The eight coefficients A_i, B_i, C_i, D_i can be found using the boundary conditions: no-slip at the interface between the bottom film and the substrate, continuity of the velocity (no-slip) and stress across the liquid/liquid interface, and no shear at the liquid/air interface. The non-linear terms of the curvature of the Laplace pressure are neglected, as well as the non-linear terms of the normal and tangential vectors of the interfaces. This means that this model would be valid in the limit of small slopes. The boundary condition implications and their resulting effect are listed below:

$$w_1 = 0 \quad \rightarrow \quad \tilde{\psi}_1 = 0, \quad z = 0. \quad (\text{C5a})$$

$$u_1 = 0 \quad \rightarrow \quad \left(\frac{d}{dz}\right) \tilde{\psi}_1 = 0, \quad z = 0. \quad (\text{C5b})$$

$$w_2 = w_1 \quad \rightarrow \quad -ik\tilde{\psi}_2 = -ik\tilde{\psi}_1, \quad z = h_1. \quad (\text{C5c})$$

$$u_2 = u_1 \quad \rightarrow \quad -\left(\frac{d}{dz}\right) \tilde{\psi}_1 = -\left(\frac{d}{dz}\right) \tilde{\psi}_2, \quad z = h_1. \quad (\text{C5d})$$

$$\eta_2(\partial_z u_2 + \partial_x w_2) = \eta_1(\partial_z u_1 + \partial_x w_1) \quad \rightarrow \quad \eta_1 \left(\left(\frac{d}{dz}\right)^2 \psi_1 + k^2 \psi_1 \right) = \eta_2 \left(\left(\frac{d}{dz}\right)^2 \psi_2 + k^2 \psi_2 \right), \quad z = h_1. \quad (\text{C5e})$$

$$\begin{aligned} -(p_1 - p_2) + 2\partial_z(\eta_1 w_1 - \eta_2 w_2) &= -\gamma_1 \partial_x^2 h_1 \quad \rightarrow \\ \eta_1 \left(3k^2 \left(\frac{d}{dz}\right) \tilde{\psi}_1 - \left(\frac{d}{dz}\right)^3 \tilde{\psi}_1 \right) - \eta_2 \left(3k^2 \left(\frac{d}{dz}\right) \tilde{\psi}_2 - \left(\frac{d}{dz}\right)^3 \tilde{\psi}_2 \right) &= ik^3 \gamma_1 \tilde{h}_1, \quad z = h_1. \end{aligned} \quad (\text{C5f})$$

$$\eta_2(\partial_z u_2 + \partial_x w_2) = 0 \quad \rightarrow \quad \left(\frac{d}{dz}\right)^2 \psi_2 + k^2 \psi_2 = 0, \quad z = h_2. \quad (\text{C5g})$$

$$-p_2 + 2\eta_2 \partial_z w_2 = -\gamma_2 \partial_x^2 h_2 \quad \rightarrow \quad \eta_2 \left(3k^2 \left(\frac{d}{dz}\right) \tilde{\psi}_2 - \left(\frac{d}{dz}\right)^3 \tilde{\psi}_2 \right) = ik^3 \gamma_2 \tilde{h}_2, \quad z = h_2. \quad (\text{C5h})$$

The Stokes equation with respect to the x -direction has been used to replace \tilde{p}_i .

$$\partial_x p = \eta_i (\partial_x^2 u_i + \partial_z^2 u_i) \quad \rightarrow \quad -ik\tilde{p}_i = \eta_i (k^2 \tilde{\psi}_i' - \tilde{\psi}_i'''). \quad (\text{C6})$$

The governing equation for the temporal evolution of the thickness profiles can be found using the kinematic condition

$$\partial_t h_i + u_i \partial_x h_i = w_i, \quad (\text{C7})$$

where u_i and w_i are evaluated at $z = h_i$. This solution is highly non-linear and very complex. However, to stay consistent with the approach of keeping only the linear terms of the governing equation we linearize the interface profile. This allows for an analytical solution. The linearization of the kinematic conditions yields to

$$\partial_t \delta \tilde{h}_1 = \tilde{w}_1(z = \bar{h}_1) = s_{11}^S \delta \tilde{h}_1 + s_{12}^S \delta \tilde{h}_2, \quad (\text{C8a})$$

$$\partial_t \delta \tilde{h}_2 = \tilde{w}_2(z = \bar{h}_1 + \bar{h}_2) = s_{21}^S \delta \tilde{h}_1 + s_{22}^S \delta \tilde{h}_2, \quad (\text{C8b})$$

and thus share the same general solution as the asymptotic model developed in the theoretical section. The growth rates $S_{i,j}$ are not written here but can be found using a formal calculation software.

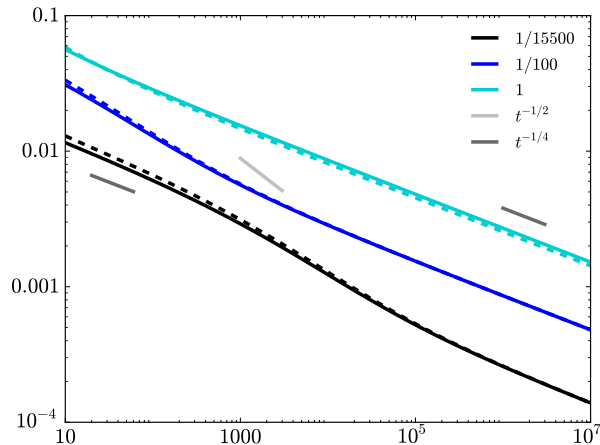


FIG. 5. A comparison of the energy dissipation as calculated by the Asymptotic model (solid) and Stokes model (dashed). Each model has been calculated over the experimental time scale and for the three viscosity ratios that were studied in this paper.

Figure 5 displays the capillary energy of the liquid/air interface for the asymptotic model (solid lines) and the Stokes model (dashed lines) at the three viscosity ratios reported in the main text. These two models are in excellent agreement in the full range of the experiment. We can notice that a small discrepancy is observed at a moderate viscosity ratio, $\eta = 1$, at large times, and another one at early times for low viscosity ratio. For the first one, we argue that the rescaling of the viscosity ratio is no longer valid, this would lead to neglecting terms in the asymptotic expansion that would otherwise affect the energy. The overall scaling is not affected by this assumption, but the exact prefactor is. The second discrepancy comes from the Stokes model: the growth rates $s_{i,j}^S$ are positive (instability) for large wave number which is nonphysical and would disappear in a model without the small slope approximation.

This Stokes model is a powerful tool to treat linear hydrodynamic model without any scaling assumption.

-
- [1] A. Oron, S. Davis, and S. Bankoff, *Rev. Mod. Phys.* **69**, 931 (1997).
 - [2] P. G. de Gennes, *CR Acad Sci II*, **308**, 1401 (1989).
 - [3] P. G. de Gennes and F. Brochard-Wyart, *CR Acad Sci II*, **310**, 1169 (1990).
 - [4] F. Brochard-Wyart and P. G. de Gennes, *CR Acad Sci II*, **317**, 13 (1990).
 - [5] J. Koplik and J. Banavar, *Phys. Rev. Lett.* **96** (2006).
 - [6] L. Xu, H. Zhang, and T. Shi, *Polymer* **99**, 185 (2016).
 - [7] P. Poesio, A. Damone, and O. K. Matar, *Physical Review Fluids* **2**, 044004 (2017).
 - [8] S. Merabia and J. Bonet Avalos, *Phys. Rev. Lett.* **101** (2008).
 - [9] R. Zhao and C. Macosko, *J. Rheolo.* **46**, 145 (2002).
 - [10] P. de Gennes, F. Brochard-Wyart, and D. Quéré, *Capillarity and Wetting Phenomena: Drops, Bubbles, Pearls, Waves* (Springer, New York, 2003).
 - [11] Z. Fakhraei and J. Forrest, *Science* **319**, 600 (2008).
 - [12] Y. Chai, T. Salez, J. McGraw, M. Benzaquen, K. Dalnoki-Veress, E. Raphaël, and J. Forrest, *Science* **343**, 994 (2014).
 - [13] K. Paeng, S. Swallen, and M. Ediger, *J. Am. Chem. Soc.* **133**, 8444 (2011).
 - [14] G. Reiter, *Phys. Rev. Lett.* (1992).
 - [15] L. Xu, D. Bandyopadhyay, T. Shi, L. An, A. Sharma, and S. Joo, *Polymer* **52**, 4345 (2011).
 - [16] A. Münch, B. Wagner, and T. P. Witelski, *Journal of Engineering Mathematics* **53**, 359 (2005).
 - [17] S. Jachalski, D. Peschka, A. Münch, and B. Wagner, *Journal of Engineering Mathematics* **86**, 9 (2014).
 - [18] O. Bäümchen, M. Benzaquen, T. Salez, J. McGraw, M. Backholm, P. Fowler, E. Raphaël, and K. Dalnoki-Veress, *Phys. Rev. E* **88** (2013).
 - [19] E. Rognin, S. Landis, and L. Davoust, *Phys. Rev. E* **84** (2011).
 - [20] M. Backholm, M. Benzaquen, T. Salez, E. Raphaël, and K. Dalnoki-Veress, *Soft Matter* **10**, 2550 (2014).

- [21] J. McGraw, T. Salez, O. Bäümchen, E. Raphaël, and K. Dalnoki-Veress, *Phys. Rev. Lett.* **109** (2012).
- [22] T. Salez, J. McGraw, O. Bäümchen, K. Dalnoki-Veress, and E. Raphaël, *Phys. Fluids* **24** (2012).
- [23] M. Benzaquen, T. Salez, and E. Raphaël, *The European Physical Journal E* **36**, 82 (2013).
- [24] M. Benzaquen, P. Fowler, L. Jubin, T. Salez, K. Dalnoki-Veress, and E. Raphael, *Soft Matter* **10**, 8608 (2014).
- [25] D. Acheson, *Elementary Fluid Dynamics* (Oxford University Press, New York, 1990).
- [26] T. Erneux and S. H. Davis, *Physics of Fluids A: Fluid Dynamics* **5**, 1117 (1993).
- [27] M. Ilton, M. Couchman, C. Gerbelot, M. Benzaquen, P. Fowler, H. Stone, E. Raphaël, K. Dalnoki-Veress, and T. Salez, *Phys. Rev. Lett.* **117** (2016).
- [28] J. McGraw, N. Jago, and K. Dalnoki-Veress, *Soft Matter* **7**, 7832 (2011).
- [29] S. Wu, *J. Phys. Chem* **74**, 632 (1970).
- [30] S. Jachalski, A. Münch, and B. Wagner, *WIAS Preprint* **2187** (2015).
- [31] R. Huang and Z. Suo, *International Journal of Solids and Structures* **39**, 1791 (2002).
- [32] M. Rivetti, V. Bertin, T. Salez, C.-Y. Hui, C. Linne, M. Arutkin, H. Wu, E. Raphaël, and O. Bäümchen, *Phys. Rev. Fluids* **2**, 094001 (2017).

Conclusions

Fluid dynamics is the study of fluid flow. It is a complex but powerful field of study, that describes fluid motion from nanoscale flow in thin films to galaxies merging together. However, flow along a boundary of a fluid body still has many fundamental questions remaining, particularly in the context of the type of boundary conditions present. In this thesis, I have presented a project that examines the boundary layer flow when thin polymer films are subject to a liquid-liquid boundary condition.

In Chapter 3, the effect of a liquid-liquid boundary condition on thin film polymer flow was studied in the context of capillary levelling. We tracked the energy dissipation in the system by examining the change in capillary energy of a stepped polymer film stacked on another immiscible polymer film. The capillary energy is proportional to the surface area of the interface, and by measuring the interface with atomic force microscopy, we can accurately calculate the capillary energy of the system. Furthermore, the hidden liquid-liquid interface was also measured by removing the top layer of polymer step with a selective solvent to simultaneously track how the two interfaces evolve. Through the power law associated with energy dissipation, we have elucidated the flow mechanisms for the two thin films. We have also examined the effect of the viscosity ratio between the top film and the bottom film on energy dissipation. This chapter was limited to one combination of polymers, and therefore

the effect of surface tension and interfacial tension ratios was not explored. Additionally, freestanding bilayer liquid films instead of supported films may yield interesting results.

Bibliography

- [1] D. J. Acheson. *Elementary Fluid Dynamics*. Oxford University Press, 1990.
- [2] R. V. Craster and O. K. Matar. Dynamics and stability of thin liquid films. *Rev. Mod. Phys.*, 81:1131–1198, 2009.
- [3] S. Dhawan and R. Narasimha. Some properties of boundary layer flow during the transition from laminar to turbulent motion. *J. Fluid. Mech.*, 3:418–436, 1958.
- [4] R. B. Bird, R. C. Armstrong, and O. Hassager. *Dynamics of polymeric liquids*, volume 1. Wiley, 1 edition, 1977.
- [5] R. Phillips, J. Kondev, J. Theriot, and H. Garcia. *Physical Biology of the Cell*. Garland Science, 2012.
- [6] O. K. C. Tsui and T. P. Russell, editors. *Polymer Thin Films*. World Scientific Publishing Co., 2008.
- [7] A. Oron, S. Davis, and S. Bankoff. Long-scale evolution of thin liquid films. *Rev. Mod. Phys.*, 69(3):931–980, 1997.

-
- [8] J. T. Koberstein. Polymer surface and interfaces. *MRS Bulletin*, pages 16–18, January 1996.
- [9] L. Xu, T. Shi, and An L. The competition between the liquid-liquid dewetting and the liquid-solid dewetting. *J. Phys. Chem*, 130(184903), 2009.
- [10] M. Rivetti, V. Bertin, T. Salez, C. Y. Hui, C. Linne, M. Arutkin, H. Wu, E. Raphaël, and O. Bäümchen. Elastocapillary levelling of thin viscous films on soft substrates. *Phys. Rev. Fluids*, 2:094001, Sep 2017.
- [11] S. Jachalski, D. Peschka, A. Münch, and B. Wagner. Impact of interfacial slip on the stability of liquid two-layer polymer films. *Journal of Engineering Mathematics*, 86(1):9–29, 2014.
- [12] J. Dutcher, K. Dalnoki-Veress, B. G. Nickel, and C. B. Roth. Instabilities in thin polymer films: From pattern formation to rupture. *Macromol. Symp.*, 159:143–150, 2000.
- [13] J. Koplik and J. R. Banavar. Slip, immiscibility, and boundary conditions at the liquid-liquid interface. *Phys. Rev. Lett.*, 96(044505), 2006.
- [14] P. G. de Gennes. *Scaling Concepts in Polymer Physics*. Cornell University Press, 1979.
- [15] R.A.L. Jones. *Soft Condensed Matter*. Oxford University Press, 2002.
- [16] G. Strobl. *The Physics of Polymers: Concepts for Understanding Their Structures and Behavior*. Springer, 2007.

-
- [17] M. Rubenstein and R. Colby. *Polymer Physics*. Oxford University Press, New York, 2003.
- [18] E. Donth. Characteristic length of glass transition. *J. Non-Cryst. Solids*, 131-133:204–206, 1991.
- [19] J. Brandrup, E. H. Immergut, and E. A. Grulke. *Polymer Handbook*. Wiley, 4 edition, 1999.
- [20] M. Sferrazza, C. Xiao, R.A.L. Jones, D. G. Bucknall, J. Webster, and J. Penfold. Evidence for capillary waves at immiscible polymer/polymer interfaces. *Phys. Rev. Lett.*, 78(19), 1997.
- [21] R. Schnell, M. Stamm, and C. Creton. Direct correlation between interfacial width and adhesion in glassy polymers. *Macromolecules*, 31:2284–2292, 1998.
- [22] E. Guyon, J.-P. Hulin, L. Petit, and C. D. Matescu. *Physical Hydrodynamics*. Oxford University Press, Oxford, 2 edition, 2012.
- [23] T. Salez, J. McGraw, O. Bäumchen, K. Dalnoki-Veress, and E. Raphaël. Capillary-driven flow induced by a stepped perturbation atop a viscous film. *Phys. Fluids*, 24(102111), 2012.
- [24] P. G. de Gennes, F. Brochard-Wyart, and D. Quere. *Capillarity and Wetting Phenomena: Drops, Bubbles, Pearls, Waves*. Springer, 2002.
- [25] F. J. Almgren Jr. and J. E. Taylor. The geometry of soap films and soap bubbles. *Scientific American*, 235:82–93, 1976.

- [26] Y. Pomeau and E. Villermaux. Two hundred years of capillarity research. *Physics Today*, pages 39–44, March 2006.
- [27] M. A. White. *Physical Properties of Materials*. CRC Press, Boca Raton, 2 edition, 2012.
- [28] S. Wu. Surface and interfacial tensions of polymer melts. 11. poly(methylmethacrylate), poly(n-butylmethacrylate) and polystyrene. *J. Phys. Chem*, 74:632–638, 1970.
- [29] H. E. Huppert. The propagation of two-dimensional and axisymmetric viscous gravity currents over a rigid horizontal surface. *J. Fluid. Mech.*, 121:43–58, 1982.
- [30] J. McGraw, T. Salez, O. Bäümchen, E. Raphaël, and K. Dalnoki-Veress. Self-similarity and energy dissipation in stepped polymer films. *Phys. Rev. Lett.*, 109:128303, Sep 2012.
- [31] L. Xu, D Bandyopadhyay, T. Shi, L. An, A. Sharma, and S.W. Joo. Dewetting kinetics of thin polymer bilayers: Role of under layer. *Polymer*, 52:4345–4354, 2011.
- [32] A. Münch, B.A. Wagner, and T. P. Witelski. Lubrication models with small to large slip lengths. *Journal of Engineering Mathematics*, 53(3-4):359–383, 2005.
- [33] F. Brochard-Wyart, P. Martin, and C. Redon. Liquid/liquid dewetting. *Langmuir*, 9:3682–3690, 1993.
- [34] P. Lambooy, K. C. Phelan, O. Haugg, and G. Krausch. Dewetting at the liquid-liquid interface. *Phys. Rev. Lett.*, 76(7), 1996.

- [35] L. Xu, D. Bandyopadhyay, A. Sharma, and S.W. Joo. Switching of interfacial instabilities from the liquid/air interface to the liquid/liquid interface in a polymer bilayer. *Soft Matter*, 7:8056–8066, 2011.
- [36] M. Ilton, M. Couchman, C. Gerbelot, M. Benzaquen, P. Fowler, H. Stone, E. Raphaël, K. Dalnoki-Veress, and T. Salez. Capillary leveling of freestanding liquid nanofilms. *Phys. Rev. Lett.*, 117:167801, Oct 2016.
- [37] J. McGraw, N. Jago, and K. Dalnoki-Veress. Capillary levelling as a probe of thin film polymer rheology. *Soft Matter*, 7:7832–7838, 2011.
- [38] T. Salez, J. McGraw, S. L. Cormier, O. Bäümchen, K. Dalnoki-Veress, and E. Raphaël. Numerical solutions of thin-film equations for polymer flows. *Eur. Phys. J. E*, 35(114), 2012.
- [39] D. Peschka, S. Bommer, S. Jachalski, R. Seeman, and B. Wagner. Impact of energy dissipation on interface shapes and on rates for dewetting from liquid substrates. *In prep.*
- [40] O. Bäümchen, M. Benzaquen, T. Salez, J. McGraw, M. Backholm, P. Fowler, E. Raphaël, and K. Dalnoki-Veress. Relaxation and intermediate asymptotics of a rectangular trench in a viscous film. *Phys. Rev. E*, 88(035001), 2013.
- [41] M. Benzaquen, P. Fowler, L. Jubin, T. Salez, K. Dalnoki-Veress, and E. Raphael. Approach to universal self-similar attractor for the levelling of thin liquid films. *Soft Matter*, 10:8608–8614, 2014.
- [42] A. Aradian, E. Raphaël, and P. G. de Gennes. “marginal pinching” in soap films. *Europhys. Lett.*, 55:834–840, 2001.

-
- [43] D. B. Hall, P. Underhill, and J. M. Torkelson. Spin coating of thin and ultrathin polymer films. *Poly. Eng. Sci.*, 38(12), 1998.
- [44] M. Backholm, M. Benzaquen, T. Salez, E. Raphaël, and K. Dalnoki-Veress. Capillary levelling of a cylindrical hole in a viscous film. *Soft Matter*, 10:2550–2558, 2014.
- [45] M. Benzaquen, T. Salez, and E. Raphaël. Intermediate asymptotics of the capillary-driven thin-film equation. *Eur. Phys. J. E*, 36(82), 2013.